Energy
Advances

PAPER

View Article Online
View Journal | View Issue

Cite this: *Energy Adv.*, 2026, **5**, 487

Unfolding the potential of the $AgSbSe_2$ chalcogenide for advancements in solar cell and photodetector technologies

Mst Zerin Zafrin Nizu,[a] Bipanko Kumar Mondal, *[a] Md. Abdur Rashid,[b] Sangita Rani Basu[c] and Jaker Hossain *[d]

Received 7th November 2025,
Accepted 8th February 2026

DOI: 10.1039/d5ya00322a

rsc.li/energy-advances

The significance of employing a singular, multifunctional material in solar cells and photodetectors has increased due to its substantial impact on device performance. This study presents the design guidelines and an inclusive simulation of high-performance chalcogenide $AgSbSe_2$-based solar cells and photodetectors using SCAPS-1D for the first time. Through a comprehensive analysis, the potential of multifunctional optoelectronic applications is highlighted by combining an n-CdS window layer with three back surface field (BSF) materials: $Al_xGa_{1-x}Sb$, FeS_2, and Cu_2SnS_3 (CTS). Among all the examined structures, the n-CdS/p-$AgSbSe_2$/p$^+$-$Al_xGa_{1-x}Sb$ configuration exhibits the highest open circuit voltage (V_{OC}) of 0.85 V and an idealized power conversion efficiency (PCE) of 34.32%, along with a fill factor (FF) of 86.64% and a short circuit current density (J_{SC}) of 46.35 mA cm^{-2}. Nevertheless, the n-CdS/p-$AgSbSe_2$/p$^+$-FeS_2 and n-CdS/p-$AgSbSe_2$/p$^+$-CTS structures exhibit PCEs of 30.37% and 30.30%, respectively, with the corresponding V_{OC} values of 0.74 V and 0.76 V, underscoring their distinct photovoltaic characteristics. Furthermore, with proper optimization, the $AgSbSe_2$-based photodetector demonstrates a remarkable responsivity of 0.81 A W^{-1} and an excellent detectivity of 2.93×10^{15} Jones at a wavelength of 1100 nm. Due to the superior band alignment of n-CdS/p-$AgSbSe_2$/p$^+$-$Al_xGa_{1-x}Sb$, a higher built-in potential of approximately 2.37 V is achieved by capacitance–voltage (C–V) analysis, which effectively enhances the maximum V_{OC} and overall efficiency of the device.

1. Introduction

Solar cell technology has emerged as one of the most extensively researched renewable energy sources, attracting significant attention amid the global transition from fossil-based energy systems. To accomplish solar cell objectives, researchers have investigated a variety of solar technologies, such as wafer-based, thin film-based, and organic-based technologies. Solar energy is revolutionized by thin film solar cells because of their incredibly thin, foldable shape and great low-light performance. Although initially limited to laboratory research, crystalline silicon technology has seamlessly transitioned to commercialization and now dominates about 90% of the global solar panel market.[1] In December 2023, LONGi's heterojunction back contact (HBC) cell achieved an efficiency of 27.09%.[2] The indirect bandgap of silicon solar cells poses serious constraints since it results in a low absorption coefficient, necessitating the use of thicker wafers for effective light capture. Furthermore, their fabrication is expensive and energy-intensive due to the extraordinarily high temperatures required for their construction, which frequently surpass 1150–2000 °C.[3] However, thin film solar cells (TFSCs) have recently attracted substantial research interest because of their cost-effective production, improved structural flexibility, enhanced adaptivity, and perceived high efficiency, which qualify them as an effective substitute for photovoltaic (PV) systems based on silicon.[4–6] Newly developed thin film photovoltaic materials have shown considerable enhancements in efficiencies. Particularly, CdTe and CIGS solar cells have demonstrated certified PCEs of over 22%.[7,8] In addition, Sb_2Se_3 and $CuInSe_2$ solar cells exhibit 10.12% and 15% PCE, respectively.[9] Despite their optimal efficiency, CdTe and CIGS solar cells are plagued by issues that prevent their large-scale integration. CdTe contains toxic cadmium, posing a threat to the environment, while CIGS relies on rare indium and selenium, driving up production costs. Both of them also degrade more easily than silicon,

---

[a] *Department of Electrical and Electronic Engineering, Begum Rokeya University, Rangpur, 5400, Bangladesh. E-mail: bipanko.apee14@gmail.com*
[b] *Department of Physics, University of Rajshahi, Rajshahi 6205, Bangladesh*
[c] *Department of Electrical and Electronic Engineering, University of Chittagong, Chattogram 4331, Bangladesh*
[d] *Photonics & Advanced Materials Laboratory, Department of Electrical and Electronic Engineering, University of Rajshahi, Rajshahi 6205, Bangladesh. E-mail: jak_apee@ru.ac.bd*

undermining their long-term stability. Therefore, it is important to develop non-toxic chalcogenide and perovskite materials to fabricate solar cells that are both long-lasting and efficient. These materials offer sustainable alternatives to lead-based systems while preserving their advantageous optoelectronic properties, including adjustable bandgaps and high absorption coefficients. Recent studies conducted in 2025 demonstrated that a lead-free $CaZrS_3$ perovskite can achieve a simulated efficiency exceeding 20%. A separate study on chalcogenide-based materials also showed that Sb_2S_3/SnS_2 heterojunctions have perfect band alignment and very little recombination loss, which makes them even more likely to have high theoretical efficiencies.[10,11] These findings highlight the increased significance of environmentally benign chalcogenides.

In this regard, silver antimony selenide ($AgSbSe_2$) is an innovative chalcogenide material that demonstrates significant potential and high efficiency. The material exhibits an optimal bandgap and carrier transport characteristics, potentially improving the performance of solar cells. $AgSbSe_2$ is a p-type semiconductor belonging to the I–V–VI_2 group of chalcogenides.[12,13] The material has a high absorption coefficient of 10^4 cm^{-1} and a Seebeck coefficient of 320 $\mu V K^{-1}$ at room temperature (300 K).[13,14] Moreover, recent studies show that the Seebeck coefficient values may be higher than previously thought, reaching about 431–462 $\mu V K^{-1}$ at higher temperatures.[15,16] $AgSbSe_2$'s tunable $\sim$1 eV bandgap, elevated hole mobility of 1500 $cm^2 V^{-1} s^{-1}$, outstanding electrical mobility, and ultra-low thermal conductivity render it ideally suited for thermoelectric, solar, and optoelectronic applications.[14,17] Furthermore, silver (Ag) and antimony (Sb) atoms occupy the metal sublattice positions in $AgSbSe_2$ thin films, which mostly have a cubic crystal structure with the space group $Fm\bar{3}m$. Nevertheless, tetragonal formations have also been observed in this compound.[13,18] Hence, it is a promising contender for next-generation energy technologies due to its stability, ecological footprint, and compatibility with flexible electronics. Additionally, $AgSbSe_2$ stands out among chalcogenides due to its unique cubic crystal structure, contrasting sharply with the low-symmetry structures commonly found in many other chalcogenides. Strong structural symmetry yields isotropic electrical and charge-transport characteristics, which are advantageous for uniform carrier collection and permit easier film-orientation criteria in thin-film solar cells. In addition, the symmetric lattice of $AgSbSe_2$ can accept certain defects, leading to a reduced impact of defect-type variations on its electrical characteristics.[19,20] Conversely, Sb_2Se_3 possesses a quasi-one-dimensional crystal structure that results in considerable transport anisotropy, rendering the device performance very orientation-dependent.[21] Besides, Cu_2SnS_3 exhibits significant cation disorder and phase complexity, resulting in major fluctuations in its electrical characteristics and overall performance.[22] Meanwhile, $AgBiSe_2$ comprises bismuth, which raises concerns about its toxicity and phase instability; its electrical characteristics are also markedly sensitive to cation ordering.[23] Although $AgSbSe_2$ has been extensively studied for thermoelectric applications, its potential in photovoltaics is mostly unexamined, underscoring the necessity for rigorous exploration in optoelectronic applications.

Furthermore, a few experimental studies have been conducted on $AgSbSe_2$ PV structures. For example, a fabricated $CdS/AgSbSe_2$ device was reported to have a J_{SC} of 0.08 mA cm^{-2} and a V_{OC} of approximately 0.435 V.[14] Additionally, the fabricated $CdS/Sb_2S_3/AgSbSe_2$ photovoltaic structure exhibited a V_{OC} of 550 mV and a J_{SC} of 2.3 mA cm^{-2}, resulting in a PCE of 0.4%.[24] Recently, an $AgSbSe_2$-based PV device achieved the best efficiency of 3.51% at low light intensities.[25] All the results indicate that the performance levels still fall significantly short of the ideal limit. Consequently, comprehensive investigations must be conducted on $AgSbSe_2$ to enhance the performance of the $AgSbSe_2$-based devices owing to its robust optoelectronic features.

However, a photodetector is an electronic apparatus that facilitates the detection of ultraviolet (UV), infrared (IR), or visible electromagnetic radiation, subsequently converting it into electrical signals.[26] Typically operating from visible to near-infrared wavelengths, photodetectors are frequently utilized in optical communication systems, optical interconnections, motion detection, the automobile sector, astronomy and space exploration, and medical imaging.[27,28] It has been reported that, for visible and near-infrared (NIR) light detection, a bandgap of around 1 eV to 2.5 eV is ideal for photodetection.[29] Up to now, most reported photodetectors—such as PbS/TiS_3, $MAPbI_3$, $CsPbI_3$, and MoS_2/Si—have exhibited detectivities in the range of 7.5×10^{10} to 3.9×10^{13} Jones and responsivities between 0.3 and 0.6 A W^{-1}.[30] However, the instability of perovskite materials limits their practical use; in this regard, $AgSbSe_2$, with its suitable bandgap, high responsivity, and excellent electrical properties, has emerged as a promising alternative for photodetector applications.

Besides, there are various methods for depositing $AgSbSe_2$ thin films, for instance, heating a Sb_2S_3–Ag stack,[17] colloidal synthesis of monodisperse $AgSbSe_2$ nanocrystals,[31] hot-injection synthesis of $Sb_2Se_3/AgSbSe_2$ hybrid nanorods,[32] and sequential deposition and annealing of polycrystalline $AgSbSe_2$.[33] To the best of our knowledge, few studies have been conducted on $AgSbSe_2$ despite its great potential in photovoltaics. As a consequence, an extensive simulation of $AgSbSe_2$ is performed in this study to investigate its enormous potential in optoelectronic devices.

In this research, a double heterostructure solar cell and photodetector are utilized, where $AgSbSe_2$ is employed as the base layer and CdS serves as the window layer, contributing to enhanced device efficiency. CdS is known as an n-type material, and utilizing it as a window layer in a photovoltaic device exhibits power and favourable semiconductor properties for its wider bandgap of 2.4 eV.[34]

Furthermore, $Al_xGa_{1-x}Sb$, FeS_2, and Cu_2SnS_3 have been systematically investigated to assess their suitability and comparative effectiveness as BSF layers in the $AgSbSe_2$-based device structures. The ternary alloy $Al_xGa_{1-x}Sb$ is composed of two binary compounds: AlSb and GaSb. This ternary compound has attracted a lot of attention recently since it can be utilized in sophisticated near- and medium-infrared optoelectronic devices by engineering the band offset and band gap. To date, $Al_xGa_{1-x}Sb$ thin films have been deposited using methods such as molecular beam epitaxy (MBE), liquid phase epitaxy (LPE), and thermal evaporation.[35] This ternary alloy has already been utilized as a BSF layer in wafer-based silicon solar cells, and its excellent carrier collection efficiency helps reduce recombination losses.[35,36] Additionally, the $Al_xGa_{1-x}Sb$ alloy shows promise as a bottom cell absorber in tandem devices.[37] However, it may also serve as a viable option for the BSF layer alongside $AgSbSe_2$ due to its superior band alignment.

Besides, FeS_2 and CTS exhibit direct band gaps of 0.95 eV and 1.07 eV, respectively, and both have identical electron affinities of 4.00 eV.[35,38] These properties enable them to function effectively as a p^+-type BSF layer in conjunction with $AgSbSe_2$, forming an optimal p/p^+-heterostructure. In general, the electrically conductive properties and inadequate reflectivity of FeS_2 and CTS are lower than those of traditional BSF materials, like silicon nitride (SiN) or aluminum (Al).[39] Moreover, the FeS_2 thin film has garnered considerable attention from the scientific community due to its impressive minority carrier diffusion length, which ranges from 100 to 1000 nm. Additionally, its low cost, non-toxicity, and exceptionally high absorption coefficient (10^5 cm^{-1}) contribute to its appeal.[35] The material has previously been used as an absorber layer, achieving an experimental efficiency of only about 3% due to its lower V_{OC}.[40] However, it may also have the potential to function effectively as a BSF layer when combined with $AgSbSe_2$. Besides, CTS is identified as a p-type semiconductor with a variable bandgap ranging from 0.92 to 1.77 eV and an optical absorption coefficient exceeding 10^4 cm^{-1}. Due to these optoelectronic properties, it holds significant potential for applications in visible-light–driven photocatalytic and photovoltaic processes.[41] Experimental studies have indicated a conversion efficiency of approximately 1.35% when CTS is used as the light-absorbing layer.[42] Additionally, its advantageous band structure and carrier characteristics make it suitable for forming a p/p^+ junction with $AgSbSe_2$, allowing it to function effectively as a BSF layer. This configuration enhances charge confinement and reduces recombination at the rear interface. CTS has recently shown its potential as a BSF layer with $CuSbSe_2$ in a tandem solar device.[43]

Therefore, in this study, $AgSbSe_2$-based photovoltaic and photodetector devices were systematically designed and analysed in detail. The SCAPS-1D simulation results demonstrate their strong potential for high-performance double heterojunction solar cell applications, as well as their capability to optimize the responsivity and detectivity of $AgSbSe_2$ for efficient photodetection.

2. Device design and computational approach

Fig. 1(a) indicates the diagrammatic architecture, and 1(b) is the energy band structure of the lighted state for the proposed $AgSbSe_2$ are both depicted in Fig. 1. In this investigation, CdS is used as a window layer, and $Al_xGa_{1-x}Sb$, FeS_2, and CTS are utilized as BSF layers. In this scheme, photons penetrate the window layer of CdS before being observed by $AgSbSe_2$. The electron affinity (E.A.) and ionization potential (I.P.) of this p-type $AgSbSe_2$ layer are 4.12 eV and 5.12 eV, respectively. For the window layer, E_C is 4.2 eV and E_V is 6.6 eV. The bandgap (E_G) and E.A. of the $Al_xGa_{1-x}Sb$ alloy are determined by employing a linear interpolation method between the corresponding values of AlSb and GaSb. The equations below illustrate how the composition of the alloy (X) relates to E_G and E.A. according to Vegard's law:[37]

$$E_{G_{Al_xGa_{1-x}Sb}} = XE_{G_{AlSb}} + (1-X)E_{G_{GaSb}} \tag{1}$$

$$\text{E.A.}_{Al_xGa_{1-x}Sb} = X\text{E.A.}_{AlSb} + (1-X)\text{E.A.}_{GaSb} \tag{2}$$

The $Al_xGa_{1-x}Sb$ compound is optimized in this study using eqn (1) and (2), and $Al_{0.8}Ga_{0.2}Sb$ is identified as the most suitable option for use as a BSF layer with $AgSbSe_2$. The

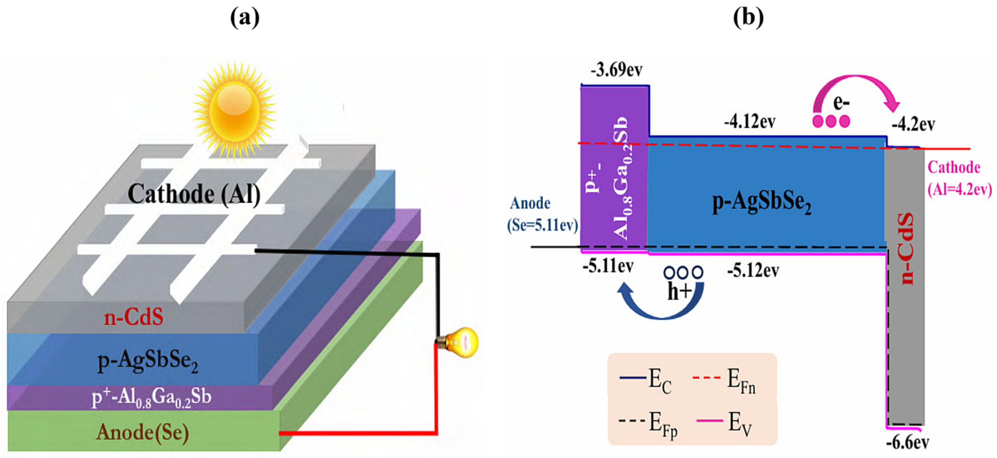

Fig. 1 (a) Methodical design and (b) electronic band layout of the $AgSbSe_2$-based device.

bandgap and electron affinity values are considered in this calculation: 0.72 eV and 4.06 eV for GaSb and 1.60 eV and 3.60 eV for AlSb, respectively.[37] However, $Al_{0.8}Ga_{0.2}Sb$ alloy shows good band alignment with $AgSbSe_2$, which makes the junction highly effective.

At the adjacent side, $Al_{0.8}Ga_{0.2}Sb$, FeS_2, and CTS have E.A. and I.P. of 3.69 eV and 5.11 eV, 4.00 eV and 4.95 eV, and 4.00 eV and 5.07 eV, respectively.[35,44] These values imply that the heterojunctions formed among the p-type absorber $AgSbSe_2$, n-type window CdS and p^+-type BSFs ($Al_{0.8}Ga_{0.2}Sb$, FeS_2 and CTS) exhibit well-aligned energy bands, promoting efficient charge carrier separation and transport. Moreover, the lattice compatibility analysis indicates that $Al_{0.8}Ga_{0.2}Sb$ (cubic, a = 6.13 Å) and FeS_2 (cubic, a = 5.4195 Å) have a close lattice match with $AgSbSe_2$ (cubic, a = 5.786 Å), suggesting minimal lattice mismatch and favorable conditions for epitaxial interface formation. In contrast, Cu_2SnS_3 (monoclinic, a = 6.653 Å, b = 11.537 Å, and c = 6.665 Å) displays slightly larger lattice discrepancies; however, its compatible band alignment stability still supports the formation of stable heterojunctions.[20,36,45,46] In addition to lattice compatibility, these chalcogenides and antimonide compounds exhibit comparable thermal expansion coefficients and demonstrate high phase stability under typical low-temperature processing conditions (less than 350 °C). This reduces the risk of interdiffusion or degradation at the interfaces.[47] Such favourable structural and thermal compatibility enhances the practical feasibility of integrating $AgSbSe_2$ with $Al_{0.8}Ga_{0.2}Sb$, FeS_2, and Cu_2SnS_3 in upcoming experimental implementations.

The illuminated electronic band diagram shown in Fig. 1(b) is drawn considering $Al_{0.8}Ga_{0.2}Sb$ as the BSF layer. Moreover, in Fig. 1(b), the dashed lines labelled as E_{Fn} and E_{Fp} represent the quasi-Fermi levels of electrons and holes, respectively. The present diagram clearly illustrates that in the window, the E_{Fp} is located below the edge of the conduction band (CB), while in the BSF, the E_{Fn} is situated above the edge of the valence band (VB). Due to this effect, the electrons generated by light absorption in the absorber layer $AgSbSe_2$ naturally move toward the window layer CdS, and holes drift to the BSF, facilitating effective carrier transport within the device. Table 1 presents the band offset values for each studied structure. The evaluated conduction band offset (ΔE_C) and valence band offset (ΔE_V) values offer helpful details about interfacial carrier dynamics within the studied heterojunctions. For the CdS/$AgSbSe_2$ interface, a small ΔE_C (0.08 eV) facilitates smooth electron transport, while a large ΔE_V (1.48 eV) effectively blocks holes, thereby minimizing recombination at the n-type window interface. The $AgSbSe_2$/FeS_2 (ΔE_C = 0.10 eV, ΔE_V = 0.13 eV) and $AgSbSe_2$/CTS (ΔE_C = 0.11 eV, ΔE_V = 0.0488 eV) junctions demonstrate nearly ideal band alignment with minimal energy barriers, which enables balanced carrier transport and efficient current matching between junctions.

Table 1 Band offset values of all the structures

Junction	ΔE_C	ΔE_V
CdS/$AgSbSe_2$	0.08	1.48
$AgSbSe_2$/$Al_{0.8}Ga_{0.2}Sb$	0.44	0.02
$AgSbSe_2$/FeS_2	0.1	0.13
$AgSbSe_2$/CTS	0.11	0.0488

Despite a relatively large conduction band offset (ΔE_C = 0.44 eV), the $AgSbSe_2$/$Al_{0.8}Ga_{0.2}Sb$ interface achieves the highest V_{OC} among the structures investigated. This phenomenon can be attributed to the suppression of interfacial recombination due to the higher potential barrier for electron back-transfer, while the minimal ΔE_V (0.02 eV) aids hole transport across the junction. Consequently, the $AgSbSe_2$/$Al_{0.8}Ga_{0.2}Sb$ heterointerface presents a favourable trade-off between charge selectivity and recombination control, resulting in enhanced V_{OC} performance.

The conception of the proposed device in this study is simulated using SCAPS-1D, a one-dimensional solar cell simulation tool often used for analyzing layered semiconductor structures, developed by M. Burgelman and co-workers at the University of Ghent, Belgium.[48–50] In this model, a bulk defect density of 10^{14} cm^{-3} was assigned to the window and BSF layers and 10^{13} cm^{-3} to the absorber layer, which were categorized as either donor or acceptor types based on semiconductor polarity (p-type or n-type) to utilize a Gaussian energy distribution. Moreover, an interface defect density of 10^{10} cm^{-2} was applied uniformly to each interface of the device due to the lattice mismatch between the different layers. Additionally, the carrier capture cross-sections were established at 10^{-15} cm^2 for all layers. As well, 10^7 cm s^{-1} was allocated as the thermal velocity for both electrons and holes. To ensure conformity with common real-world photovoltaic performance benchmarks, the simulation was run using conventional test settings, such as an illumination intensity of 1000 W cm^{-2} and the AM1.5G sun spectrum. In Table 2, the physical parameters for the window,[51] absorber[14,17,52,53] and three different BSF layers in detail[35,44] used in this simulation are shown. Carrier concentrations and overall device behaviour are largely determined by the effective density of states for the valence band N_V and the conduction band N_C. To ensure precise modelling of the semiconductor properties, these absorber layer parameters were assessed using conventional equations that rely on temperature and the effective masses of electrons and holes.[44] These values are calculated using the following equations:

$$N_C = 2\left(\frac{m_e^* K_B T}{2\pi h^2}\right)^{3/2} \tag{3}$$

$$N_V = 2\left(\frac{m_h^* K_B T}{2\pi h^2}\right)^{3/2} \tag{4}$$

In this work, the effective masses of electrons $\left(m_e^*\right)$ and holes $\left(m_h^*\right)$ in $AgSbSe_2$ are considered to be 0.26 m_0 and 1.2 m_0, respectively.[52,54] In addition, h is the Planck's constant, K_B is the Boltzmann constant, and T is the absolute temperature in Kelvin (300 K is used here).

In addition, as the key performance metrics in this investigation, responsivity and detectivity provide a profound

Table 2 Material parameters of $AgSbSe_2$, window and BSF layers incorporated in the simulation

Parameters	n-CdS[51]	p-$AgSbSe_2$[14,17,52,53]	p^+-$Al_{0.8}Ga_{0.2}Sb$[35]	p^+-FeS_2[35]	p^+-CTS[44]
Bandgap, E_g (eV)	2.40	1.00	1.42	0.95	1.07
Electron affinity, E.A. (χ) (eV)	4.2	4.12	3.69	4.00	4.00
Dielectric permittivity, ε (relative)	10.0	7.981	12.04	10.0	10.00
CB effective density of states, N_C (cm^{-3})	2.2×10^{18}	3.33×10^{18}	7.8×10^{17}	3×10^{18}	2.2×10^{18}
VB effective density of states, N_V (cm^{-3})	1.8×10^{19}	3.29×10^{19}	1.8×10^{19}	3×10^{19}	1.8×10^{19}
Mobility of electron, μ_e ($cm^2 V^{-1} s^{-1}$)	100	417.4[52]	200	370	100
Hole mobility, μ_h ($cm^2 V^{-1} s^{-1}$)	2500	1500[17]	420	70	25
Shallow uniform donor density, N_D ($1/cm^3$)	1×10^{18}	0	0	0	0
Shallow uniform acceptor density, N_A ($1/cm^3$)	0	1×10^{19} (ref. 53)	1×10^{19}	1×10^{19}	1×10^{19}

understanding of the effectiveness and sensitivity of the developed photonic device. Both are necessary for assessing and maximizing the overall performance of the photodetector device. These can be determined using the following eqn (5) and (6):[55,56]

$$\text{Detectivity}\,(D) = \frac{R}{\sqrt{2 \times j_0 \times q}}, \tag{5}$$

$$\text{Responsivity}\,(R) = \frac{q \times \eta \times \lambda}{h \times c}, \tag{6}$$

where λ denotes the wavelength, η represents the quantum efficiency (QE), h is Planck's constant, j_0 denotes the dark current, q is the charge of an electron and c denotes the speed of light. The calculated dark current was extremely small, about 2.4×10^{-13} mA cm^{-2}, which is typical for high quality photodetectors and solar cells.

Besides, the J_{SC}, V_{OC}, FF, and PCE values determine the principal electrical photovoltaic characteristics of a solar cell. J_{SC} represents the maximum current output when the terminals of the solar cell are short-circuited, resulting in a voltage of zero. V_{OC} denotes the maximum voltage measurable across a solar cell under open-circuit conditions, where the current equals zero. Additionally, J_{SC} can be defined based on the light absorption and the probability of collecting carriers:[57]

$$J_{SC} = f_c \int_0^{\lambda_m} q\Phi \text{AM1.5G}(\lambda) A^1(\lambda)\,d\lambda, \tag{7}$$

where A^1 represents the one pass absorption, f_c represents the carrier collecting probability, and ΦAM1.5G(λ) represents the incoming light flux. The relationship between J_{SC} and V_{OC} can be expressed as follows:

$$V_{OC} = \frac{KT}{q} \ln\left(\left(\frac{J_{SC}}{J_0}\right) + 1\right), \tag{8}$$

where K represents the Boltzmann constant, T denotes the absolute temperature, q denotes the elementary charge, and J_0 denotes the saturation current density. FF can be expressed as

$$\text{FF} = \frac{P_{max}}{V_{OC} \times J_{SC}}, \tag{9}$$

where $P_{max} = V_m \times I_m$, and at the maximum power point, V_m is the voltage and I_m is the current.

Moreover, efficiency can be defined as follows:

$$\text{PCE} = \frac{J_{SC} V_{OC} \text{FF}}{P_{in}} \tag{10}$$

where P_{in} = input power.

3. Results and discussion

3.1. Performance of the CdS/$AgSbSe_2$ solar cell

This analysis explores how structural and material changes within the $AgSbSe_2$ absorber and CdS window layer, specifically in terms of width, dopant levels, and intrinsic defect states, impact the electrical performance of the proposed n-CdS/p-$AgSbSe_2$ heterojunction-based solar configuration.

3.1.1. Role of $AgSbSe_2$ as an absorber layer. Fig. 2 provides a visual representation of how altering the thickness and doping concentration of the absorber influences the photovoltaic response, as presented through contour plots. Fig. 2(a) illustrates that J_{SC} exhibits a notable enhancement, increasing from 33.76 mA cm^{-2} to 47.43 mA cm^{-2} as the absorber thickness is varied from 0.3 μm to 1.1 μm. As thickness increases, more photons are absorbed, resulting in elevated electron–hole pair density and a higher photocurrent, which makes the increase in J_{SC} feasible.[58] However, doping level variations also significantly affect performance, which moderately decreases the value, indicating that increasing free carrier density enhances free-carrier absorption and non-radiative recombination, which reduces the effective current density in this regime.[59]

The variation in V_{OC} corresponding to the changes in absorber width and carrier density is depicted in Fig. 2(b), which reflects the cell's electrical behaviour. The minimum V_{OC} of 0.62 V is observed at a lower thickness of 0.3 μm and a concentration of 1×10^{16} cm^{-3} doping levels, indicating that optimal doping levels are critical to maintaining higher voltage outputs. V_{OC} remains nearly constant with increasing thickness at this doping level. In contrast, a noticeable increase in V_{OC} is observed with higher doping concentrations. A peak V_{OC} of 0.67 V is achieved at an absorber thickness of 1.1 μm combined with a doping concentration of 1×10^{20} cm^{-3}. An increase in absorber thickness within the tested range has a negligible effect on V_{OC}, while it increases with higher doping concentration as a result of improved built-in potential and reduced recombination losses.[60]

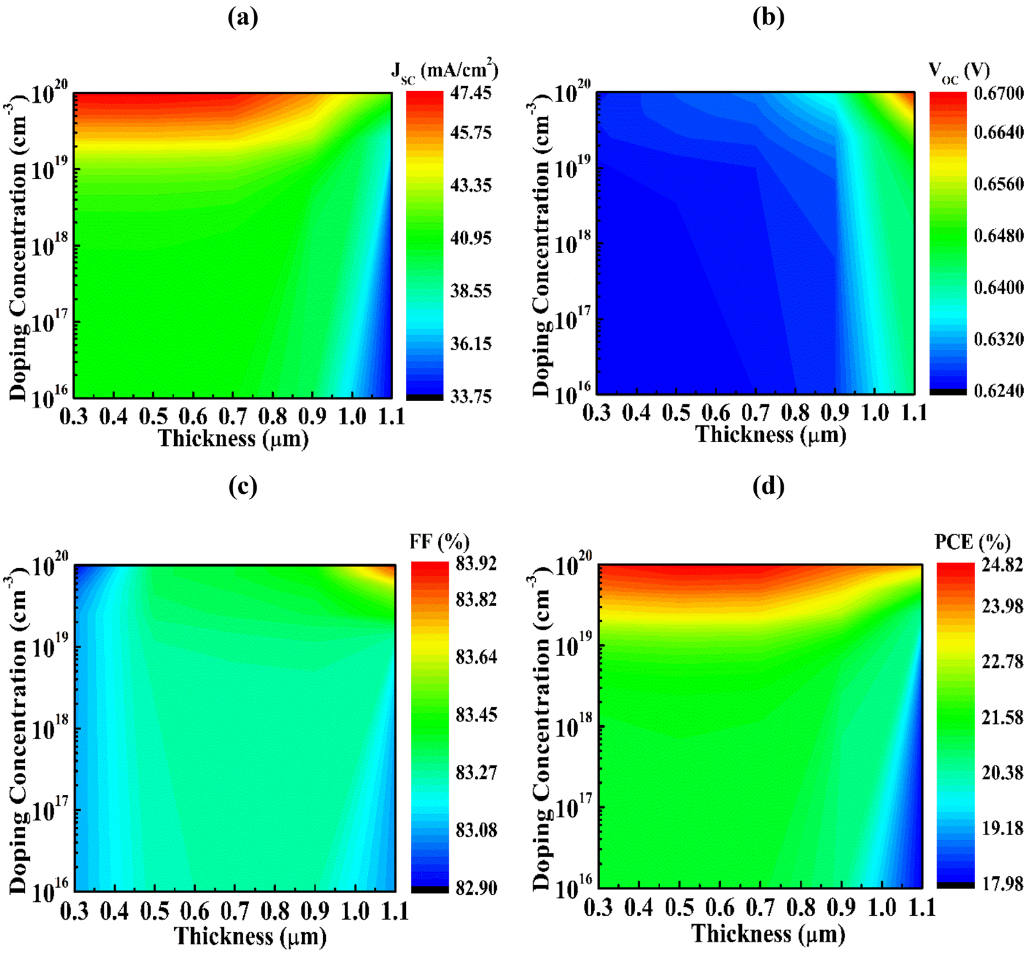

Fig. 2 Analyses of the (a) J_{SC}, (b) V_{OC}, (c) FF, and (d) PCE of the CdS/AgSbSe$_2$ PV device in accordance with the thickness and doping of AgSbSe$_2$.

As shown in Fig. 2(c), both the greater thickness and higher doping concentration of the AgSbSe$_2$ absorber contribute to maintaining a stable FF. Along the thickness range from 0.3 μm to 1.1 μm, FF shows minimal sensitivity, which is only a small variation from 83.06% to 82.9%. However, it slightly increases to 83.92% at the highest doping level of 10^{20} cm^{-3} due to the drops in the ideality factor.[61] Fig. 2(d) depicts that with a thickness of 0.3 μm, PCE is approximately 21.16%. As the thickness attains 1.1 μm with a doping concentration of 10^{17} cm^{-3}, PCE reaches a maximum value of 24.82%. Meanwhile, a substantial increase in doping density from 10^{16} cm^{-3} to 10^{20} cm^{-3} leads to a reduction in PCE to 23.67% at the same thickness of 1.1 μm.

The contour plots in Fig. 3 systematically illustrate the dependence of key photovoltaic characteristics on variations in both the thickness and intrinsic defect concentration of the absorber, offering insights into their combined influence on device performance. According to Fig. 3(a), J_{SC} remains relatively low at 39.51 mA cm^{-2} for small absorber thicknesses and shows a negligible decrease with variations in bulk defect density. As the thickness increases, J_{SC} begins to rise gradually, reaching a maximum value of 45.50 mA cm^{-2}.

Fig. 3(b) demonstrates a steady increase in V_{OC} with increasing absorber, rising from 0.62 V at 0.3 μm to a peak of 0.63 V at 1.1 μm. However, it remains almost stable with variations in defect density within the range of 10^{11}–10^{15} cm^{-3}. Despite increasing absorber defect density, V_{OC} remains nearly constant because recombination is dominated by interface or depletion-region effect rather than bulk defects. Since charge generation and collection are unaffected, quasi-Fermi level splitting does not change, resulting in an almost invariant V_{OC}.

In Fig. 3(c), FF remains constant with increasing defect density up to 10^{14} cm^{-3}, attaining its maximum value of 83.43%. After that, FF again starts to fall marginally with bulk defects. However, it exhibits slight growth with the width of the absorber. The variation of FF in accordance with the bulk defects might occur due to the change in the ideality factor.[62] Fig. 3(d) illustrates that PCE initially increases with absorber thickness, rising from 20.62% at 0.3 μm to a maximum of 24.21% at 1.1 μm; although at the same thickness, it declines to 24.15% when the defect density increases to 10^{15} cm^{-3}. This demonstrates that while thickness improves performance, high defect density has an adverse effect. The optimized values for the width, carrier level, and defects of AgSbSe$_2$ are identified as

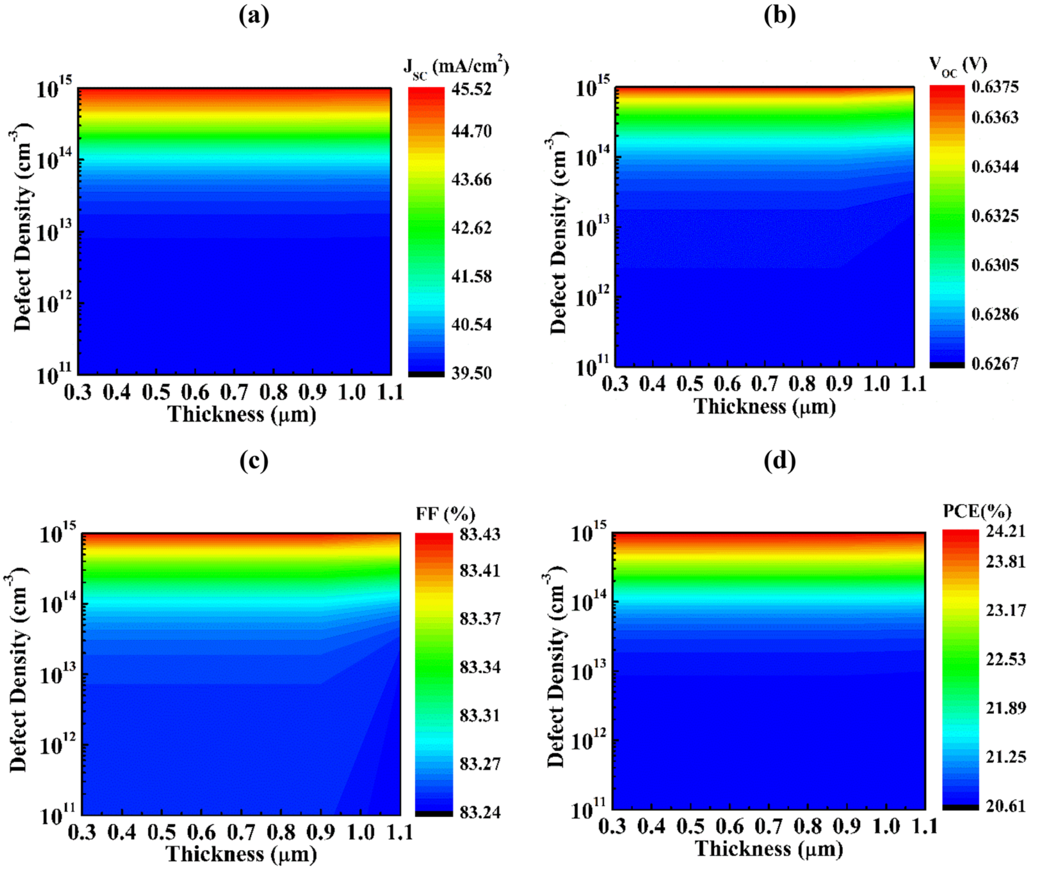

Fig. 3 Analyses of the (a) J_{SC}, (b) V_{OC}, (c) FF, and (d) PCE of the CdS/AgSbSe$_2$ PV device in accordance with the thickness and defect density of AgSbSe$_2$.

0.7 µm, 10^{19} cm^{-3}, and 10^{13} cm^{-3}, respectively, for further investigations.

3.1.2. Contribution of CdS as a window layer. From the data depicted in Fig. 4(a), it is clear that adjusting the thickness within the range of 0.05–0.25 µm of the CdS window layer produces little to no impact on V_{OC}, which remains approximately constant at ~0.63 V. This can be explained by the inherent wide bandgap of CdS, which prevents significant

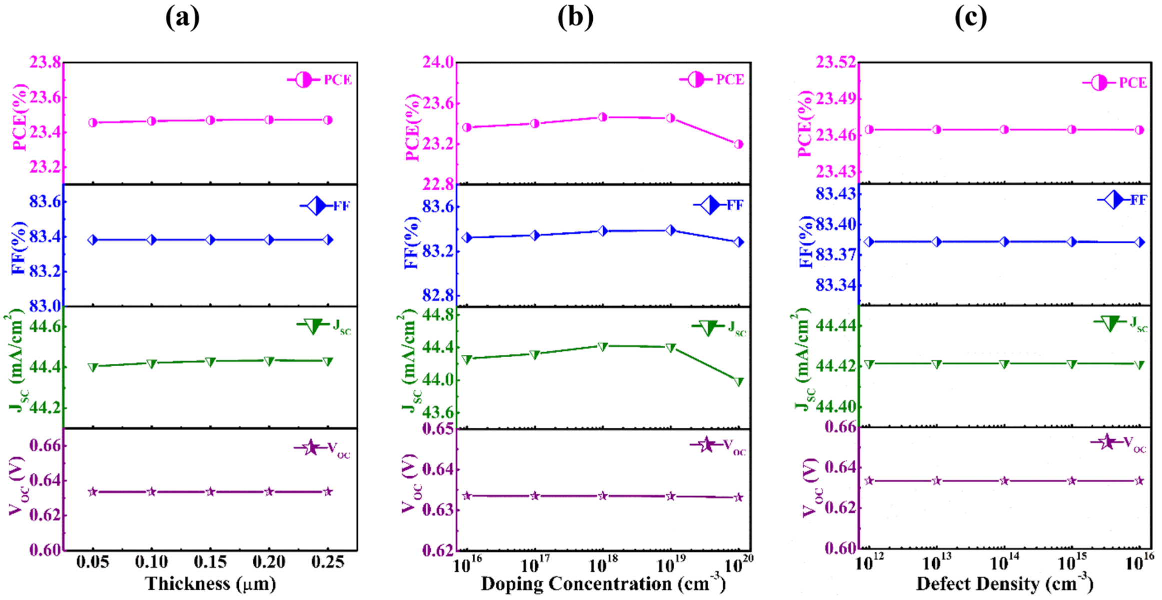

Fig. 4 Photovoltaic performance assessment of the CdS/AgSbSe$_2$ heterostructure in relation to the (a) width, (b) donor level, and (c) bulk defects of CdS.

absorption losses, thus allowing optimal light penetration to the active region. J_{SC} initially exhibits a value of 44.40 mA cm^{-2} and shows a negligible increase to about 44.43 mA cm^{-2} as the thickness reaches 0.15 μm. In contrast, PCE and FF remain unaffected by the variation in thickness, maintaining values of approximately 23.4% and 83.38%, respectively. Throughout the investigated thickness range, the CdS window layer exhibits a high carrier lifetime and diffusion length. Because of this trait, electrons can quickly reach the cathode before they recombine, which keeps the device working properly.[63]

Fig. 4(b) shows the influence of varying CdS doping concentrations from 10^{16} to 10^{20} cm^{-3} on the performance of the n-CdS/p-AgSbSe$_2$ solar cell. No significant change in V_{OC} is observed here. J_{SC} shows a rising trend as doping concentration increases, up to 10^{19} cm^{-3} due to improved conductivity and enhanced carrier collection. However, at a higher level of 10^{20} cm^{-3}, it drops minimally, which can be attributed to the decreased carrier lifetime. FF exhibits a non-monotonic trend, rising from 83.32% to 83.39% at 10^{19} cm^{-3}, and starts declining from 10^{20} cm^{-3} as a result of enhanced recombination.[61] Here, PCE shows the same behaviour as J_{SC}; it increases to a level of 10^{19} cm^{-3}, then drops progressively and reaches its lowest point at higher doping levels.

In Fig. 4(c), throughout the CdS layer defect density spanning from 10^{12} to 10^{16} cm^{-3}, the parameters V_{OC}, J_{SC}, FF and PCE maintained stability within the interval values of 0.63 V, 44.42 mA cm^{-2}, 83.38%, and 23.46%, respectively. The CdS window layer's defect density has a limited effect on device performance because of its thin nature and primary role in charge transport rather than carrier generation, resulting in minimal recombination losses despite defect variations. Hence, the most appropriate values for the width, carrier concentration, and defect levels of CdS are determined to be 0.1 μm, 10^{18} cm^{-3}, and 10^{14} cm^{-3}, respectively, for subsequent studies.

3.2. Performance of the CdS/AgSbSe$_2$ heterostructures utilizing various BSF layers

In this context, the current–voltage (*J*–*V*) characteristic curves of different types of heterostructures with or without a BSF layer are shown in Fig. 5(a), where CdS and AgSbSe$_2$ are used as window and absorber layers, respectively. Fig. 5(b) illustrates the quantum efficiency (QE) of the same structures, and Fig. 5(c) illustrates the recombination rate. Here, the first figure spells out the values of V_{OC} and J_{SC} measured as 0.6334 V and 44.42 mA cm^{-2}, respectively, without any BSF layer present. After introducing different BSF layers, a noticeable variation in

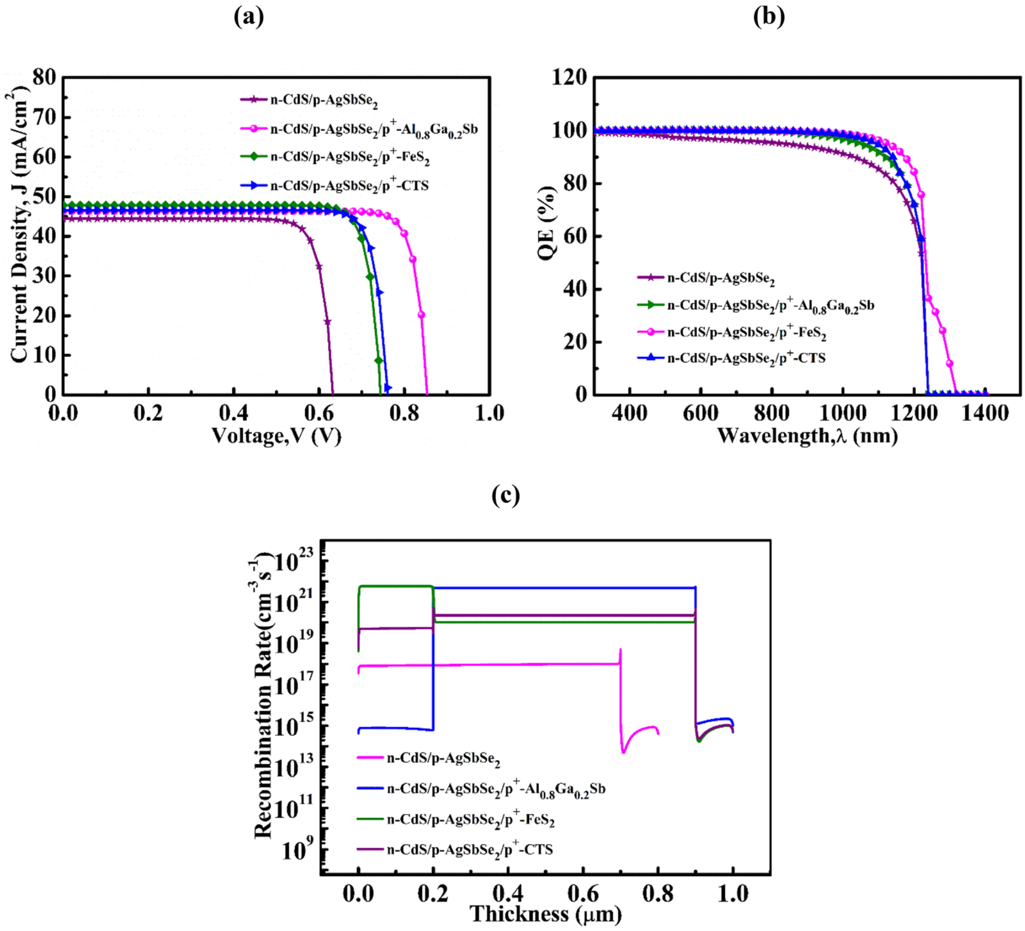

Fig. 5 (a) *J*–*V*, (b) QE, and (c) recombination profiles of various AgSbSe$_2$-based heterostructures.

V_{OC} is observed depending on the band structure of the materials. The simulation parameters for various BSF layers were utilized, as outlined in Table 2. In the dual heterostructure of CdS/AgSbSe$_2$/FeS$_2$, there is an appreciable increase in V_{OC}, reaching about 0.74 V, and in CdS/AgSbSe$_2$/CTS, it becomes 0.76 V. However, the maximum V_{OC} achieved is about 0.85 V at the CdS/AgSbSe$_2$/Al$_{0.8}$Ga$_{0.2}$Sb structure, which can be attributed to the enhanced built-in potential formed at the CdS/AgSbSe$_2$ and AgSbSe$_2$/Al$_{0.8}$Ga$_{0.2}$Sb heterostructures, highlighting how variations in band alignment across different structures critically influence V_{OC}.[64] Specifically, the optimal band offset value between AgSbSe$_2$ and Al$_{0.8}$Ga$_{0.2}$Sb increases the built-in potential, contributing to a higher V_{OC} compared to other materials. Besides, the devices with the FeS$_2$ layer exhibit a considerable improvement in J_{SC}. J_{SC} rises to 46.35 mA cm^{-2} at the CdS/AgSbSe$_2$/Al$_{0.8}$Ga$_{0.2}$Sb structure, while the value slightly rises to 46.57 mA cm^{-2} in CdS/AgSbSe$_2$/CTS. The highest J_{SC} of 47.79 mA cm^{-2} is shown by FeS$_2$ compared to the other BSF layers. The constructed current density is elevated by suppressing interface-related carrier recombination, employing the diminution of the surface recombination velocity.[56]

Due to its small bandgap of 0.95 eV, FeS$_2$ can absorb longer-wavelength photons ranging from 1240 to 1316 nm. This capability contributes to an increase in the current to nearly 1 mA cm^{-2} when compared to CTS and Al$_{0.8}$Ga$_{0.2}$Sb. The device FF is greatly impacted by the choice of BSF arrangement. The reference n-CdS/p-AgSbSe$_2$ device shows an FF of 83.38%, while FeS$_2$ and CTS layers increase FF to 85.30% and 85.49%, respectively, although p$^+$ BSFs are preferred for superior performance. The enhanced FF results from increased carrier mobility, longer carrier lifetimes, and decreased recombination, all of which improve carrier collecting efficiency. The slightly higher FF in Al$_{0.8}$Ga$_{0.2}$Sb at 86.64% is attributed to ideal band alignment at the absorber and BSF interface, which reduces series resistance and enhances charge transport and diode quality.

In Fig. 5(b), QE is shown with respect to the wavelength. QE measures how effectively a solar cell can transform incoming photons into charge carriers, and its value changes across various wavelengths as a result of the material's absorption properties.[65] Without the BSF layer, the QE reaches around 99.2% at a wavelength range of 300–360 nm and continuously decreases. Furthermore, at 1240 nm, it becomes zero due to being devoid of photon absorption. When every incoming photon is transformed into electric charges, the maximum photon absorption capability occurs at 100%. After adding the BSF layer, the QE reaches almost 100% in the wavelength range of 300–1000 nm, for all cases. In addition, at 1100 nm, all of the heterostructures exhibit above 90% QE. However, beyond this point, the QE of the CTS and Al$_{0.8}$Ga$_{0.2}$Sb BSF layers drops to zero at 1240 nm, while FeS$_2$ maintains a non-zero response up to approximately 1316 nm. At a wavelength of 1240 nm, the CdS/AgSbSe$_2$/FeS$_2$ device also presents a QE of 35%. This extended absorption range enables FeS$_2$ to produce an additional photocurrent of around 1 mA compared to the other two BSF-based structures. This suggests that the FeS$_2$ layer can absorb photons in the 1240–1316 nm range, which contributes to the observed increase of 1 mA in the photocurrent. Hence, it is clear that FeS$_2$ performs the dual roles of a secondary absorber and a hole transport layer in the AgSbSe$_2$-based devices.

An inspection of Fig. 5(c) reveals the recombination behaviour of AgSbSe$_2$ heterostructures incorporating different BSF layers. Recombination is the process by which electrons and holes come together and cancel each other out, which works against the effect of generation. Without a BSF layer, the CdS/AgSbSe$_2$ setup in the p-region has a very low recombination rate. When a p$^+$ layer is added, the recombination rate increases for all structures in the p-region. In addition, FeS$_2$ exhibits a higher recombination rate within the device compared to CTS and Al$_{0.8}$Ga$_{0.2}$Sb in the p$^+$-region, resulting in a significantly lower V_{OC}. In contrast, the inclusion of Al$_{0.8}$Ga$_{0.2}$Sb as a BSF in the configuration results in the most suppressed recombination rate in the p$^+$-region, out of all the examined structures. This reduced recombination facilitates a higher V_{OC} relative to other BSF structures. In AgSbSe$_2$/Al$_{0.8}$Ga$_{0.2}$Sb, the small valence band offset enables efficient hole transport across the junction, while the relatively large conduction band offset serves as an energy barrier that repels electrons from the back contact. This selective carrier confinement significantly reduces interfacial recombination. As a result, the AgSbSe$_2$/Al$_{0.8}$Ga$_{0.2}$Sb configuration promotes better carrier selectivity and enhances V_{OC} by maintaining a high quasi-Fermi level separation near the absorber/BSF interface. As a result, Al$_{0.8}$Ga$_{0.2}$Sb is identified as a more favourable BSF material for the AgSbSe$_2$-based devices. At the same time, CdS serves as an effective window layer for integration with the AgSbSe$_2$ absorber. However, in the n-region, the recombination rate in FeS$_2$ devices is notably diminished, and with CTS material designs present, nearly equivalent behaviour is observed due to the small conduction band offset, which facilitates increased electron transport. Conversely, Al$_{0.8}$Ga$_{0.2}$Sb shows slightly higher recombination on this side.

The total built-in potential (Ψ_{bi}) of the AgSbSe$_2$-based double heterostructure PV devices was calculated to assess the internal electric field across the active regions. Table 3 presents the estimated Ψ_{bi} values, derived as the sum of the built-in

Table 3 Variations in the built-in potential of AgSbSe$_2$ structures with distinct interfaces

Structures		Built-in potential (V)		
n/p	p/p$^+$	n/p	p/p$^+$	Built-in potential (total) (V)
CdS/AgSbSe$_2$	AgSbSe$_2$/Al$_{0.8}$Ga$_{0.2}$Sb	0.94	1.43	2.37
	AgSbSe$_2$/FeS$_2$		0.96	1.90
	AgSbSe$_2$/CTS		1.07	2.01

potentials at the window/absorber (p–n) and absorber/BSF (p–p^+) junctions:

$$\Psi_{\text{bi}} = \Psi_{(\text{p–n})} + \Psi_{(\text{p–p}^+)} \tag{11}$$

A mathematical expression can be used to determine the built-in voltage in a heterojunction p–n configuration:[66]

$$\psi_{(\text{p–n})} = \frac{\Delta E_{\text{C}} - \Delta E_{\text{V}}}{2q} + \frac{KT}{q}\ln\frac{N_{\text{D}}N_{\text{A}}}{n_{\text{i,n}}n_{\text{i,p}}} + \frac{KT}{2q}\ln\frac{N_{\text{v,n}}N_{\text{c,p}}}{N_{\text{c,n}}N_{\text{v,p}}} \tag{12}$$

where N_{C} and N_{V} denote the density of states of the conduction and valence bands, respectively. E_{C} and E_{V} denote the energy levels at the edges of the conduction and valence bands, respectively. The donor and acceptor doping concentrations are given by N_{D} and N_{A}, respectively. The intrinsic carrier concentrations for the n-type and p-type semiconductors are represented by $n_{\text{i,n}}$ and $n_{\text{i,p}}$. Meanwhile, q denotes the electron charge and KT denotes the thermal energy. The intrinsic carrier concentration (n_{i}) in semiconductors can be calculated from the effective densities of states and the energy gap using a specific exponential formula:[67]

$$n_{\text{i}} = \sqrt{N_{\text{V}}N_{\text{C}}}\,e^{-\frac{E_{\text{g}}}{2kT}} \tag{13}$$

where E_{g} is the energy bandgap. The provided formula is utilized to determine the potential difference established in $\Psi_{(\text{p–p}^+)}$:[68]

$$\psi_{(\text{p–p}^+)} = \frac{\Delta E_{\text{C}} - \Delta E_{\text{V}}}{2q} + \frac{KT}{q}\ln\frac{N_{\text{a}}N_{\text{A}}}{n_{\text{i,p}}n_{\text{i,p}^+}} + \frac{KT}{2q}\ln\frac{N_{\text{v,p}}N_{\text{c,p}^+}}{N_{\text{c,p}}N_{\text{v,p}^+}}. \tag{14}$$

The estimated built-in potential for each interface and total heterostructure is shown in Table 3. The calculated value of Ψ_{bi} for CdS/AgSbSe$_2$ is 0.94 V. With the incorporation of multiple BSF layers, the voltage increases noticeably, reflecting better charge confinement and improved junction potential. CdS/AgSbSe$_2$/FeS$_2$ and CdS/AgSbSe$_2$/CTS obtain built-in potentials of about 1.90 V and 2.01 V, respectively, which signifies a reduced equilibrium voltage drop across the junction, typically due to a small Fermi level difference between the adjacent layers compared to Al$_{0.8}$Ga$_{0.2}$Sb-based BSF. In opposition, CdS/AgSbSe$_2$/Al$_{0.8}$Ga$_{0.2}$Sb provides a maximum built-in potential of about 2.37 V, which leads to attaining the highest V_{OC}. The observed relatively high built-in potential of 2.37 V for this structure is attributed to the significant Fermi level difference between the moderately doped p-type AgSbSe$_2$ and the highly doped p^+-type Al$_{0.8}$Ga$_{0.2}$Sb. This pronounced doping gradient enhances band bending at the interface, resulting in a stronger internal electric field. Additionally, the small valence band offset facilitates efficient hole transport, while the higher conduction band offset creates a considerable electron barrier that reduces carrier recombination and preserves a strong internal electric field. Collectively, these characteristics contribute to a higher built-in potential compared to other CTS or FeS$_2$.[64]

3.3. Impact of Al$_{0.8}$Ga$_{0.2}$Sb as the BSF layer

The above discussions signify that the Al$_{0.8}$Ga$_{0.2}$Sb compounds perform as an optimized BSF layer with AgSbSe$_2$ absorber layer compared to others. Hence, the subsequent sections discuss the PV results on the AgSbSe$_2$ solar cells, considering CdS as the window and Al$_{0.8}$Ga$_{0.2}$Sb as the BSF layers. Fig. 6 illustrates the

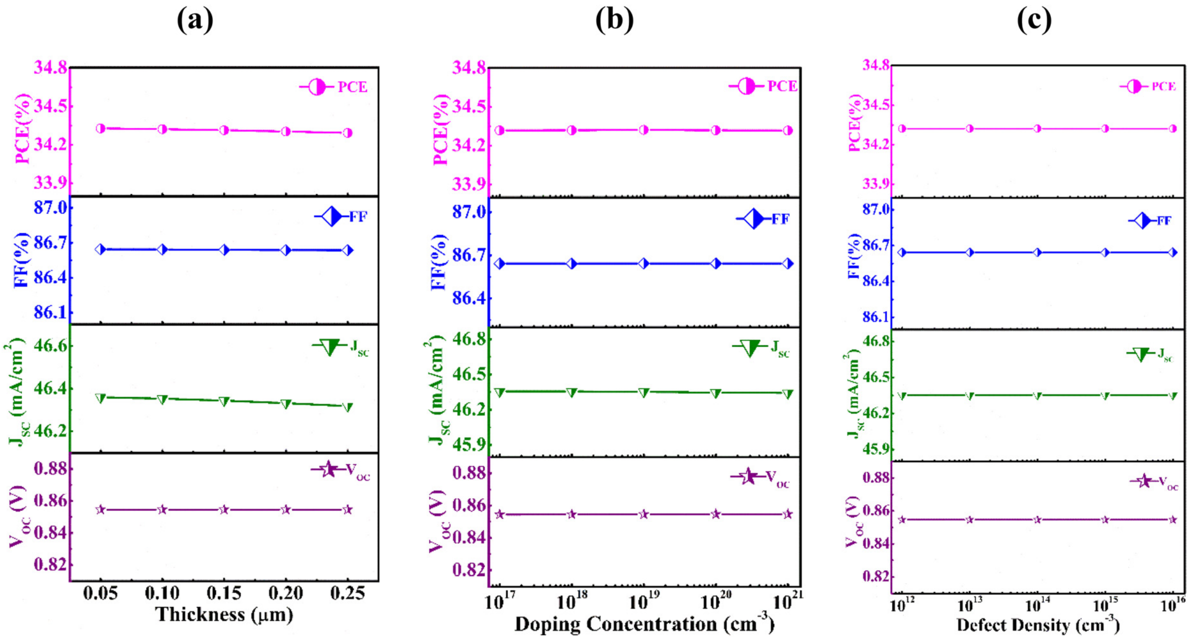

Fig. 6 Photovoltaic performance assessment of the CdS/AgSbSe$_2$/Al$_{0.8}$Ga$_{0.2}$Sb heterostructure in relation to the (a) thickness, (b) acceptor level, and (c) bulk defects of Al$_{0.8}$Ga$_{0.2}$Sb.

effect of $Al_{0.8}Ga_{0.2}Sb$ BSF layer properties, such as thickness, doping level, and defect density, on overall photovoltaic performance. The thickness of the BSF layer is observed in the range of 0.05–0.25 μm, as depicted in Fig. 6(a). In this range, the photovoltaic traits are almost constant: V_{OC} is about 0.86 V, J_{SC} stabilizes at about 46.3 mA cm^{-2}, PCE is around 34.3%, and FF is about 86.6%. This consistency indicates that device performance is not significantly affected by minor variations in BSF thickness, suggesting thickness independence in this interval. Due to the thick electrical confinement and reduced surface recombination, the BSF layer sustains a high carrier lifetime and diffusion length. This allows photogenerated carriers to efficiently reach the hole contact before recombining, thus preserving device performance across the thickness range.

As shown in Fig. 6(b), the PV parameter values here also barely alter when the doping level is changed from 10^{16} to 10^{21} cm^{-3}. J_{SC} and V_{OC} exhibit minimal fluctuations around 46.4 mA cm^{-2} and 0.86 V, respectively, while FF and PCE stay steady near 86.7% and 34.3%. Similarly, under defect density variation, all parameters remain constant and maintain values of V_{OC} around 0.85 V, J_{SC} at 46.35 mA cm^{-2}, FF at 86.6%, and PCE close to 34.3%, as shown in Fig. 6(c).

The stability of observed parameters through all changes in BSF layers demonstrates a regime of material and structural adequacy, where carrier confinement is already optimized, and additional changes become practically ineffective.

3.4. Effect of the absorber's electronic properties on performance

This subsection thoroughly evaluates the effects of defect states, carrier mobility, and band tailing of $AgSbSe_2$ on n-CdS/p-$AgSbSe_2$/p^+-$Al_{0.8}Ga_{0.2}Sb$ heterojunction device behaviour.

Fig. 7(a) illustrates how the PV performance of the CdS/$AgSbSe_2$/$Al_{0.8}Ga_{0.2}Sb$ heterostructure varies in relation to the Urbach energy (U_E) states of the $AgSbSe_2$ absorber layer. The U_E indicates the degree of band-tailing and energetic disorder present in the absorber. It primarily influences sub-bandgap absorption and carrier generation. The U_E states ranged from 0.02 to 0.1 eV. The figure shows that as the U_E of the $AgSbSe_2$ absorber rises from 0.02 to 0.1 eV, enhanced band-tail absorption allows for better utilization of low-energy photons, leading to an increase in the density of photogenerated carriers. Consequently, J_{SC} has significantly improved. Besides, V_{OC} remains nearly constant because it is governed by quasi-Fermi level splitting, which is primarily influenced by the main recombination pathways. Changes in U_E do not significantly affect the primary bulk or interface recombination mechanisms, leading to a saturation current density that remains relatively unchanged. As a result, V_{OC} stays consistent. Additionally, FF is maintained because carrier transport and series resistance do not vary much within the examined range of U_E. PCE improves to 36.41% based on the J_{SC} value within the U_E range.

Fig. 7(b) examines how all PV responses depend on various defect charge states (neutral, single donor, single acceptor,

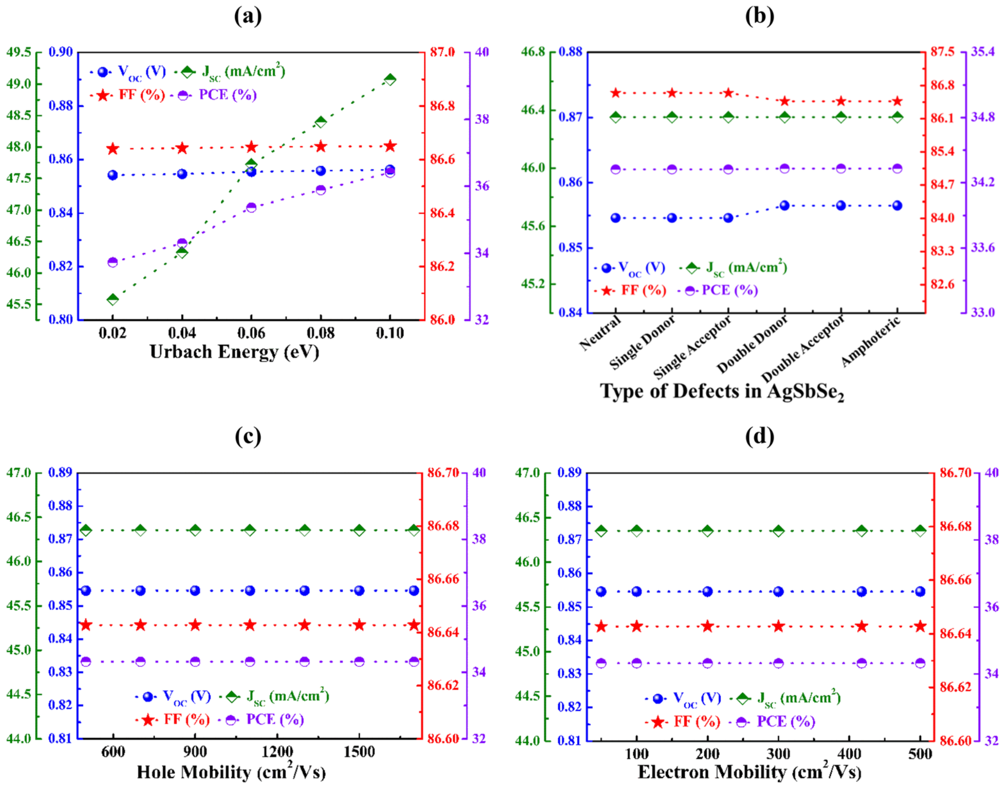

Fig. 7 Photovoltaic performance assessment of the CdS/$AgSbSe_2$/$Al_{0.8}Ga_{0.2}Sb$ heterostructure in relation to the (a) Urbach energy, (b) defect type, (c) hole mobility, and (d) electron mobility of the $AgSbSe_2$ absorber.

double donor, double acceptor, and amphoteric) in $AgSbSe_2$. The figure depicts the almost stable behaviour of all parameters associated with the $CdS/AgSbSe_2/Al_{0.8}Ga_{0.2}Sb$ device. The fact that all PV outputs remain unchanged regardless of the defect charge state (neutral, single donor, single acceptor, double donor, double acceptor, or amphoteric) in the $AgSbSe_2$ absorber indicates that the electrostatic nature of bulk defects does not constrain the device's performance. Moreover, the various defect states do not significantly alter the carrier lifetime or quasi-Fermi level splitting. This implies that recombination remains governed by processes occurring at the interface or within the depletion region rather than by the charge states of bulk defects.

Fig. 7(c) and (d) illustrate the variation in the photovoltaic (PV) performance of the $AgSbSe_2$-based device in relation to the hole and electron mobility of the absorber layer, respectively. The hole mobility ranges from 500 to 1700 $cm^2\ V^{-1}\ s^{-1}$, while the electron mobility is adjusted from 50 to 500 $cm^2\ V^{-1}\ s^{-1}$. Both figures demonstrate that the consistency of PV outputs in the proposed heterostructure correlates with the carrier mobility of $AgSbSe_2$. Changing the mobilities of electrons and holes does not affect the PV parameters, indicating that carrier transport is not the limiting factor in the $CdS/AgSbSe_2/Al_{0.8}Ga_{0.2}Sb$ device. In the range of mobilities examined, the lengths of carrier diffusion exceed the thickness of the absorber. Additionally, the built-in electric field facilitates charge collection and enhances extraction efficiency. Since mobility does not directly influence recombination or quasi-Fermi level splitting, the parameters J_{SC}, V_{OC}, FF, and PCE remain relatively unchanged.

3.5. Effect of device resistances and temperature on device performance

The electrical behaviour of solar cells is greatly influenced by internal series and parallel resistances, which primarily arise due to layer-to-layer contact resistance, electrode interconnections, and structural defects induced during device fabrication.[69]

Performance outcomes in solar cells are strongly influenced by internal resistance elements. The highest PCE is typically attained when the device exhibits minimal series resistance (R_S) and maximized shunt resistance (R_{sh}). This happens because low series resistance reduces power loss in current flow, while high shunt resistance prevents leakage currents, together maximizing the solar cell's output.[70] Fig. 8 illustrates the variations in R_S, R_{sh} and operating temperature impact the photovoltaic characteristics of the $n\text{-}CdS/p\text{-}AgSbSe_2/p^+\text{-}Al_{0.8}Ga_{0.2}Sb$ dual-heterojunction solar cell.

Fig. 8(a) illustrates that the FF and PCE of the solar cell decline noticeably as the R_S increases from 0 to 5 Ω cm^2. In contrast, both V_{OC} and J_{SC} remain largely unaffected by this variation. FF decreases from 86% to 61%. PCE is primarily attributed to the decline in FF; PCE drops from 34.3% to 24.5% as Rs increases within the specified range.

In Fig. 8(b), the solar cell's characteristics shift depending on the applied R_{sh} in the 1–5 kΩ cm^2 range. Similar to the previous observation for R_S, V_{OC} and J_{SC} remain unaffected by changes in R_{sh}. Both FF and PCE experience a minimal reduction compared to the ideal case when R_{sh} is set to 1 kΩ cm^2. An increase in R_{sh} leads to higher values of FF and PCE, which reach 86.35% and 34.2%, respectively, at 5 kΩ cm^2.

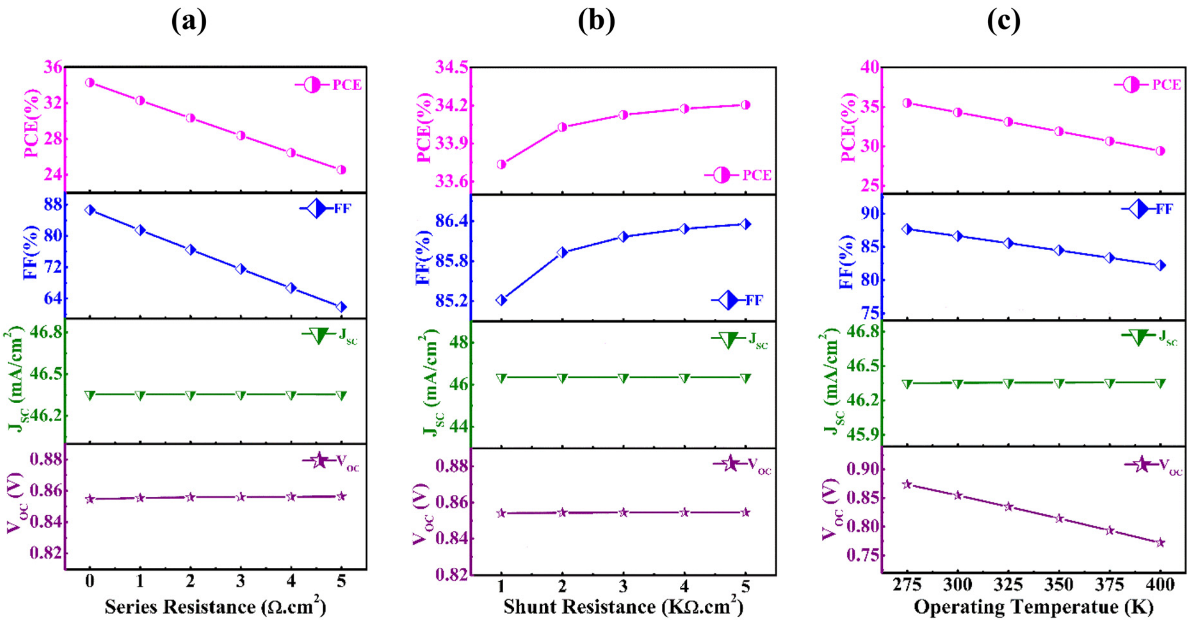

Fig. 8 Photovoltaic performance assessment of the $CdS/AgSbSe_2/Al_{0.8}Ga_{0.2}Sb$ heterostructure in relation to (a) series resistance, (b) shunt resistance, and (c) working temperature.

Fig. 8(c) shows how the solar cell's PV performance changes when the temperature changes between 275 K and 400 K. J_{SC} stays at a fairly steady level in this range of temperature. As the operating temperature rises, V_{OC} drops sharply, from 0.87 V to 0.77 V at 400 K. This decline occurs because the dark current flow increases.[23] The rise in temperature also causes a significant drop in FF, from 87.6% to 82.2%. PCE also undergoes a sharp reduction, dropping to 29.4%, primarily driven by the degradation of V_{OC} and FF across the temperature range. A higher temperature boosts the velocity of charge carriers, which lowers the bond energy and narrows the bandgap of the semiconductor. As a result, the saturation current of the solar cell rises along with the intrinsic carrier concentration.[71]

3.6. Efficacy of the $AgSbSe_2$ absorber in photodetectors

Fig. 9 illustrates how the responsivity and detectivity of the $AgSbSe_2$ photodetector are influenced by structural changes. This shows that variations in wavelength consistently impact the responsivity and detectivity performance of the device.

As shown in Fig. 9(a), the device without BSF n-CdS/p-$AgSbSe_2$ exhibits a peak responsivity of 0.76 A W^{-1} at a wavelength of 1100 nm. In comparison, the inclusion of a BSF layer significantly enhances device performance. Fig. 9(b) to (d) depict the responsivity and detectivity of CdS/$AgSbSe_2$ devices that incorporate $Al_{0.8}Ga_{0.2}Sb$, CTS, and FeS_2 BSF layers, respectively. The $Al_{0.8}Ga_{0.2}Sb$- and CTS-based devices attain peak responsivities of 0.81 A W^{-1} and 0.84 A W^{-1}, respectively,

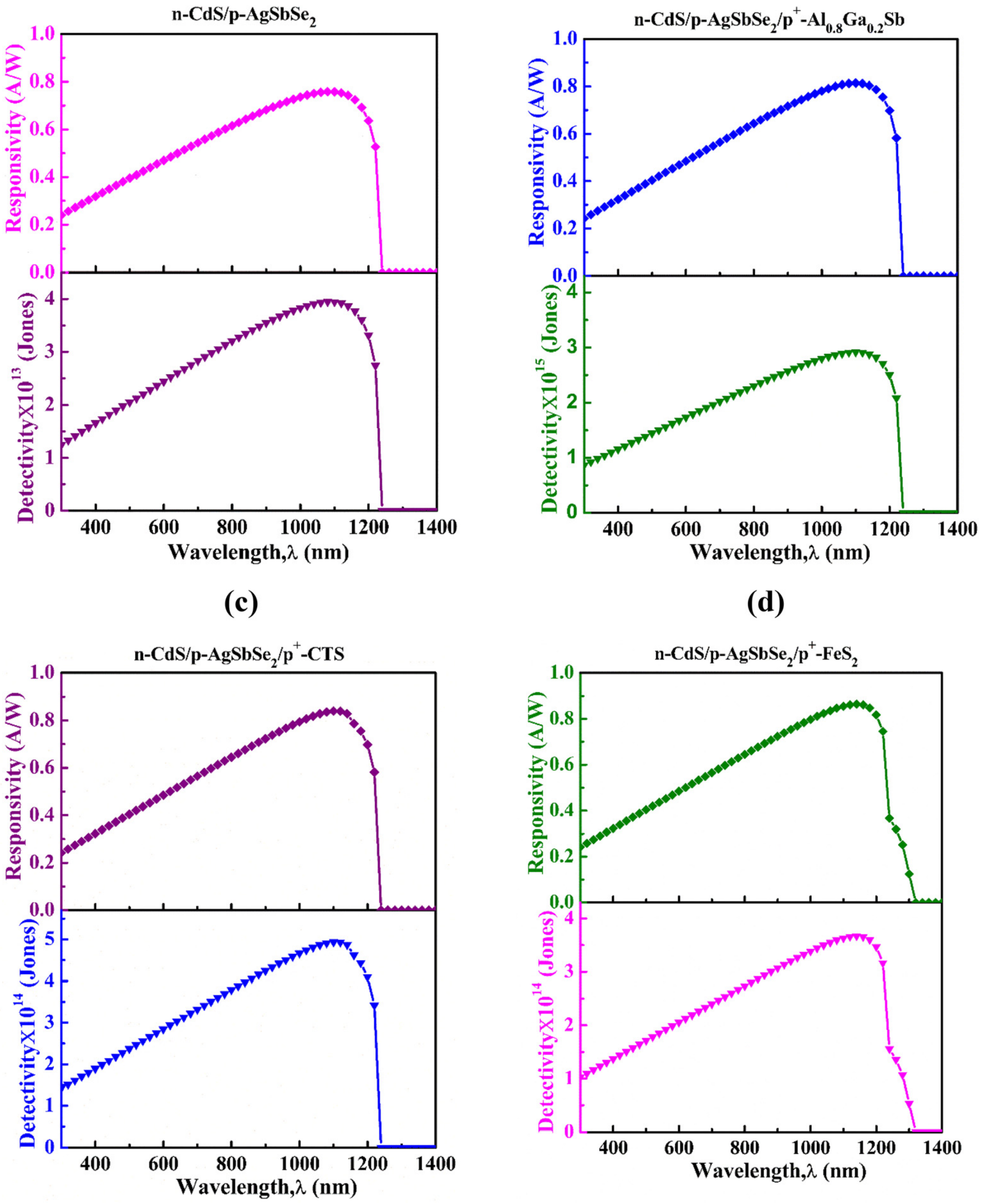

Fig. 9 Detectivity and responsivity performances of the $AgSbSe_2$-based (a) n-CdS/p-$AgSbSe_2$, (b) n-CdS/p-$AgSbSe_2$/p^+-$Al_{0.8}Ga_{0.2}Sb$, (c) n-CdS/p-$AgSbSe_2$/p^+-CTS, and (d) n-CdS/p-$AgSbSe_2$/p^+-FeS_2 photodetectors.

at the same wavelength of 1100 nm, while at the range of 1139 nm, the FeS_2-based structure achieves an improved maximum responsivity of 0.86 A W^{-1}, as displayed in Fig. 9(b)–(d). The incorporation of the BSF layer mitigates recombination, boosts charge carrier concentration and mobility, and enhances carrier collection and current generation, resulting in increased device responsivity.[30,72] It is also observed that when the wavelength exceeds 1238 nm, the photons no longer carry enough energy to excite electrons, so the photodetector stops responding. However, in this region, FeS_2 generates slightly more current due to its extended absorption range, resulting in relatively higher responsivity up to 1320 nm, beyond which the responsivity drops to zero.

At the same time, the device's detectivity, in the absence of a BSF layer, is 1.24×10^{13} Jones at 300 nm, as shown in Fig. 9(a). It progressively rises to its maximum value of 3.95×10^{13} Jones at 1079 nm. There is a noticeable increase in detectivity after adding a BSF layer. The n-CdS/p-$AgSbSe_2$/p$^+$-$Al_{0.8}Ga_{0.2}Sb$ structure, as presented in Fig. 9(b), exhibits the highest detectivity of any BSF configuration, with a reading of roughly 2.93×10^{15} Jones at 1100 nm and 0.86×10^{15} Jones at 300 nm. This happens because detectivity is inversely dependent on the square root of the dark current; both increasing V_{OC} and lowering the dark current contribute significantly to enhancing the device's detectivity.[73] Furthermore, the CTS achieves a detectivity of 4.92×10^{14} Jones at 1100 nm, whereas the FeS_2 layer shows 3.68×10^{14} Jones at 1139 nm, as shown in Fig. 9(c)–(d). These findings demonstrate that improving photodetector performance across many spectral areas requires both absorber thickness and BSF integration. However, detectivity drastically decreases to zero for wavelengths longer than 1236 nm.

3.7. Optimized performances of the $AgSbSe_2$-based solar cells and photodetectors

An overview of the $AgSbSe_2$ performance based on both single and double-heterojunction solar cells is illustrated in Table 4. At n-CdS/p-$AgSbSe_2$ interface, the device exhibits relatively lower performance. With the inclusion of the BSF layer, performance metrics, including V_{OC}, J_{SC}, responsivity, and detectivity, exhibit considerable improvement, thereby validating its role as a key enabling layer for an enhanced optoelectronic response in the device.

It is observed that the highest performance is attained in the dual-heterostructure configuration comprising n-CdS/p-$AgSbSe_2$/p$^+$-$Al_{0.8}Ga_{0.2}Sb$, as evidenced by a notable PCE of 34.32% and a V_{OC} of 0.85 V. Conversely, the n-CdS/p-$AgSbSe_2$/p$^+$-FeS_2 structure shows a lower PCE of 30.37%, along with a reduced V_{OC} of 0.74 V. Moreover, the n-CdS/p-$AgSbSe_2$/p$^+$-CTS configuration exhibits a similar PCE of 30.30% and a slightly enhanced V_{OC} of 0.76 V. Although $Al_{0.8}Ga_{0.2}Sb$ provides a better V_{OC}, the FeS_2 BSF shows a higher J_{SC} of 47.79 mA cm^{-2}. The J_{SC} values for $Al_{0.8}Ga_{0.2}Sb$ and CTS remain closely matched but relatively lower, which are measured at 46.35 and 46.57 mA cm^{-2}, respectively. FF reaches a maximum value of 86.64% for $Al_{0.8}Ga_{0.2}Sb$, while FeS_2 and CTS yield slightly lower values of 85.30% and 85.49%, respectively. However, a more recent experimental study reported a PCE of 3.51% for the $AgSbSe_2$-based devices under low-light conditions.[25] In comparison, the simulated double heterostructures presented in this work exhibit superior performance parameters. Since the reported performance of the $AgSbSe_2$-based optoelectronic devices represents a theoretical and idealized outcome derived from the assumptions inherent in the SCAPS-1D simulation model, the obtained results are likewise idealized. Additionally, in these simulations, optical losses such as reflection at interfaces and parasitic absorption in non-active layers were not explicitly accounted for. Additionally, all layers were assumed to have perfect interfaces and uniform thicknesses. Standard ohmic contacts were established as boundary conditions, and interface defects were included only where explicitly defined, utilizing realistic defect densities from previous studies. Under these idealized conditions, we neglected non-radiative recombination, series and shunt resistances, and other practical device imperfections. Therefore, the reported PCE signifies the upper theoretical limit, providing insights into intrinsic material and layer performance while recognizing that actual devices will encounter further optical and electrical losses.

However, the $AgSbSe_2$-based photodetector in the absence of any BSF layers leads to a responsivity of 0.76 A W^{-1}. In contrast, this photodetector shows comparable responsivity when integrated with different BSF layers, achieving values of 0.81 and 0.84 A W^{-1} at 1100 nm for $Al_{0.8}Ga_{0.2}Sb$ and CTS, respectively, with a peak responsivity of 0.86 A W^{-1} observed for FeS_2 at 1139 nm. Additionally, the reference CdS/$AgSbSe_2$ device without a BSF layer exhibits a detectivity of approximately 3.95×10^{13} Jones. The detectivities of CdS/$AgSbSe_2$/CTS and CdS/$AgSbSe_2$/FeS_2 double heterostructures increase up to the highest 3.68×10^{14} and 4.92×10^{14} Jones, respectively, when CTS or FeS_2 is used as the BSF layer. Notably, the CdS/$AgSbSe_2$/$Al_{0.8}Ga_{0.2}Sb$ structure achieves the highest detectivity, approaching 2.93×10^{15} Jones. This enhancement can be attributed to the BSF-induced upsurge in the built-in potential, which raises V_{OC} and facilitates efficient carrier separation and collection.

Table 4 Overall cell performances of the $AgSbSe_2$-based devices

	Solar cell performances				Photodetector performances	
Heterostructures	V_{OC} (V)	J_{SC} (mA cm^{-2})	FF (%)	PCE (%)	Detectivity (Jones)	Responsivity (A W^{-1})
n-CdS/p-$AgSbSe_2$	0.63	44.42	83.38	23.46	3.95×10^{13} at λ = 1079 nm	0.766 at λ = 1100 nm
n-CdS/p-$AgSbSe_2$/p$^+$-$Al_{0.8}Ga_{0.2}Sb$	0.85	46.35	86.64	34.32	2.93×10^{15} at λ = 1100 nm	0.819 at λ = 1100 nm
n-CdS/p-$AgSbSe_2$/p$^+$-FeS_2	0.74	47.79	85.30	30.37	3.68×10^{14} at λ = 1139 nm	0.867 at λ = 1139 nm
n-CdS/p-$AgSbSe_2$/p$^+$-CTS	0.76	46.57	85.49	30.30	4.92×10^{14} at λ = 1100 nm	0.842 at λ = 1100 nm

These findings align well with recently reported dual heterojunction photodetectors, whose detectivities typically fall in the range of 10^{15}–10^{18} Jones. For example, $Cu_2ZnGeSe_4$-based devices (I_2–II–IV–VI_4 family) exhibit a detectivity of 8.28 × 10^{17} Jones,[74] $ZnGeAs_2$ achieves 1.25 × 10^{17} Jones,[75] Fe_2GeS_4 reaches 2.74 × 10^{16} Jones,[76] and the n-ZnSe/p-$CdGeP_2$/p^+-GeS dual heterojunction device attains 3.87 × 10^{18} Jones.[77] Moreover, Ag_3AuS_3- and Ag_3AuSe_2-based photodetectors have also demonstrated detectivities of the order of 10^{15} Jones.[73,78] These comparisons confirm that the proposed $AgSbSe_2$-based double heterostructures exhibit competitive detectivity performance relative to state-of-the-art chalcogenide and I–III–VI_2 systems.

4. Conclusion

This work successfully reveals the potential of novel $AgSbSe_2$-based solar cells and photodetectors through theoretical investigation. This design manifests CdS as a window and $Al_{0.8}Ga_{0.2}Sb$, FeS_2 and CTS as BSF layers. The impact of crucial factors such as layer thickness, carrier concentration, and defect density is systematically analysed using SCAPS-1D to optimize device performance. The n-CdS/p-$AgSbSe_2$ single-junction optoelectronic device attains a PCE of 23.46%, with a J_{SC} of 44.42 mA cm^{-2}, a V_{OC} of 0.63 V, and an FF of 83.38%. With the integration of the various BSF layers, n-CdS/p-$AgSbSe_2$/p^+-$Al_{0.8}Ga_{0.2}Sb$ achieves the best photovoltaic performance among all studied structures, reaching an outstanding PCE of 34.32%, V_{OC} of 0.85 V, J_{SC} of 46.35 mA cm^{-2}, and an FF of 86.64%. Additionally, a peak responsivity of 0.819 A W^{-1} and detectivity of 2.93 × 10^{15} Jones are observed at 1100 nm for n-CdS/p-$AgSbSe_2$/p^+-$Al_{0.8}Ga_{0.2}Sb$ heterostructure, confirming its superior photodetection capability. The incorporation of the $Al_{0.8}Ga_{0.2}Sb$ BSF layer enriches the built-in potential from 0.94 to 2.37 V and boosts V_{OC}, enhancing PCE and detectivity. The superior band alignment between p-$AgSbSe_2$ and p^+-$Al_{0.8}Ga_{0.2}Sb$ hetero-interface handles augmenting V_{OC}. This research identifies n-CdS/p-$AgSbSe_2$/p^+-$Al_{0.8}Ga_{0.2}Sb$ configuration as a viable and efficient solar cell and photodetector, offering high efficiency, long-term stability, and strong potential for real-world applications.

Conflicts of interest

None of the authors have any competing financial interests.

Data availability

Data will be available from the corresponding author upon reasonable request.

Acknowledgements

The authors are highly indebted to Prof. Dr Marc Burgelman, University of Gent, Belgium, for supplying the SCAPS 1D simulator. This research has not been funded by any research organization or university.

References

1 K. L. Chopra, P. D. Paulson and V. Dutta, Thin-film solar cells: an overview, *Prog. Photovoltaics Res. Appl.*, 2004, **12**, 69–92, DOI: 10.1002/pip.541.

2 G. Wang, Q. Su, H. Tang, H. Wu, H. Lin, C. Han, T. Wang, C. Xue, J. Lu, L. Fang, Z. Li, X. Xu and P. Gao, 27.09%-efficiency silicon heterojunction back contact solar cell and going beyond, *Nat. Commun.*, 2024, **15**, 8931, DOI: 10.1038/s41467-024-53275-5.

3 I. García, *Chapter 5 - Silicon solar cell fabrication technology*, 2025, pp. 129–171, DOI: 10.1016/B978-0-323-96105-9.00005-7.

4 G. Han, S. Zhang, P. P. Boix, L. H. Wong, L. Sun and S.-Y. Lien, Towards high efficiency thin film solar cells, *Prog. Mater. Sci.*, 2017, **87**, 246–291, DOI: 10.1016/j.pmatsci.2017.02.003.

5 Q. Guo, S. J. Kim, M. Kar, W. N. Shafarman, R. W. Birkmire, E. A. Stach, R. Agrawal and H. W. Hillhouse, Development of $CuInSe_2$ nanocrystal and nanoring inks for low-cost solar cells, *Nano Lett.*, 2008, **8**, 2982–2987, DOI: 10.1021/NL802042G.

6 Y. Zhou, L. Wang, S. Chen, S. Qin, X. Liu, J. Chen, D. J. Xue, M. Luo, Y. Cao, Y. Cheng, E. H. Sargent and J. Tang, Thin-film Sb_2Se_3 photovoltaics with oriented one-dimensional ribbons and benign grain boundaries, *Nat. Photonics*, 2015, **9**, 409–415, DOI: 10.1038/nphoton.2015.78.

7 I. Dharmadasa and A. Alam, How to achieve efficiencies beyond 22.1% for CdTe-Based thin-film solar cells, *Energies*, 2022, **15**, 9510, DOI: 10.3390/en15249510.

8 K. F. Tai, R. Kamada, T. Yagioka, A. Handa, S. Adachi, T. Kato and H. Sugimoto, From 20.9% to 22.3% CIGS solar cell: reduced recombination rate at the interface and depletion region due to k-treatment, *26th International Photovoltaic Science and Engineering Conference at Singapore*, (2016) 1–3.

9 L. Stolt, J. Hedström, J. Kessler, M. Ruckh, K. O. Velthaus and H. W. Schock, ZnO/CdS/$CuInSe_2$ thin-film solar cells with improved performance, *Appl. Phys. Lett.*, 1998, **62**, 597, DOI: 10.1063/1.108867.

10 U. U. Rehman, K. U. Sahar, K. Mahmood, E. Hussain and C.-M. Wang, Exploring the potential of non-toxic chalcogenide based perovskite solar cells: performance analysis and insights, *Inorg. Chem. Commun.*, 2025, **174**, 113923, DOI: 10.1016/j.inoche.2025.113923.

11 U. U. Rehman, R. S. Almufarij, E. A. Shokralla, K. U. Sahar, A. R. Abd-Elwahed, I. Ragab, M. A. Fahmy, S. H. Alrefaee, A. Ashfaq and C.-M. Wang, Numerical design and optimization of Sb_2S_3/SnS_2 heterojunction solar cells: performance analysis and insights, *Mater. Sci. Eng. B*, 2025, **312**, 117873, DOI: 10.1016/j.mseb.2024.117873.

12 V. Vijay, S. Harish, J. Archana and M. Navaneethan, Cation disorder and bond anharmonicity synergistically boosts the thermoelectric performance of p-type $AgSbSe_2$, *CrystEngComm*, 2021, **23**, 5522–5530, DOI: 10.1039/D1CE00599E.

13 K. T. Wojciechowski, J. Tobola, M. Schmidt and R. Zybala, Structural and thermoelectric properties of $AgSbSe_2$ and $AgSbTe_2$, *11th Int. Conf. Exhib. Eur. Ceram. Soc.* **2009**. 1 (2007).

14 J. G. Garza, S. Shaji, A. C. Rodriguez, T. K. Das Roy and B. Krishnan, $AgSbSe_2$ and $AgSb(S,Se)_2$ thin films for photovoltaic applications, *Appl. Surf. Sci.*, 2011, **257**, 10834–10838, DOI: 10.1016/j.apsusc.2011.07.115.

15 Y. Liu, D. Cadavid, M. Ibáñez, J. De Roo, S. Ortega, O. Dobrozhan, M. Kovalenko and A. Cabot, Colloidal AgSbSe2 nanocrystals: surface analysis, electronic doping and processing into thermoelectric nanomaterials, *J. Mater. Chem. C*, 2016, **4**, 4756–4762, DOI: 10.1039/c6tc00893c.

16 M. Zou, Q. Liu, C. F. Wu, T. R. Wei, Q. Tan, J. F. Li and F. Chen, Comparing the role of annealing on the transport properties of polymorphous $AgBiSe_2$ and monophase $AgSbSe_2$, *RSC Adv.*, 2018, **8**, 7055–7061, DOI: 10.1039/c7ra12819c.

17 K. Bindu, J. Campos, M. T. S. Nair, A. Snchez and P. K. Nair, Semiconducting $AgSbSe_2$ thin film and its application in a photovoltaic structure, *Semicond. Sci. Technol.*, 2005, **20**, 496–504, DOI: 10.1088/0268-1242/20/6/004.

18 K. Persson, *Materials Data on $AgSbSe_2$ (SG:141) by Materials Project*, 2016, DOI: 10.17188/1206643.

19 S. N. Guin and K. Biswas, Sb deficiencies control hole transport and boost the thermoelectric performance of p-type $AgSbSe_2$, *J. Mater. Chem. C*, 2015, **3**, 10415–10421, DOI: 10.1039/C5TC01429H.

20 S. Guin, A. Chatterjee, D. Negi, R. Datta and K. Biswas, High thermoelectric performance in tellurium free p-type $AgSbSe_2$, *Energy Environ. Sci.*, 2013, **6**, 2603, DOI: 10.1039/c3ee41935e.

21 A. Mavlonov, T. Razykov, F. Raziq, J. Gan, J. Chantana, Y. Kawano, T. Nishimura, H. Wei, A. Zakutayev, T. Minemoto, X. Zu, S. Li and L. Qiao, A review of Sb_2Se_3 photovoltaic absorber materials and thin-film solar cells, *Sol. Energy*, 2020, **201**, 227–246, DOI: 10.1016/j.solener.2020.03.009.

22 V. R. Minnam Reddy, M. R. Pallavolu, P. R. Guddeti, S. Gedi, K. K. Yarragudi Bathal Reddy, B. Pejjai, W. K. Kim, T. R. R. Kotte and C. Park, Review on Cu_2SnS_3, Cu_3SnS_4, and Cu_4SnS_4 thin films and their photovoltaic performance, *J. Ind. Eng. Chem.*, 2019, **76**, 39–74, DOI: 10.1016/j.jiec.2019.03.035.

23 H. Jang, M. Y. Toriyama, S. Abbey, B. Frimpong, J. P. Male, G. J. Snyder, Y. S. Jung and M. Oh, Suppressing charged cation antisites via Se vapor annealing enables p-Type dopability in $AgBiSe_2$ –SnSe thermoelectrics, *Adv. Mater.*, 2022, **34**, 2204132, DOI: 10.1002/adma.202204132.

24 K. Bindu, M. T. S. Nair, T. K. Das Roy and P. K. Nair, Chemically deposited photovoltaic structure using antimony sulfide and silver antimony selenide absorber films, *Electrochem. Solid-State Lett.*, 2006, **9**, 195–199, DOI: 10.1149/1.2186428.

25 P. Boon-on, P.-H. Chen and M.-W. Lee, $AgSbSe_2$ nanoparticles: A solar absorber material with an optimal Shockley-Queisser band gap, *Mater. Lett.*, 2022, **309**, 131412, DOI: 10.1016/j.matlet.2021.131412.

26 Y. Zhao, C. Li and L. Shen, Recent research process on perovskite photodetectors: a review for photodetector—materials, physics, and applications, *Chin. Phys. B.*, 2018, **27**, 127806, DOI: 10.1088/1674-1056/27/12/127806.

27 Y. El-Batawy, F. M. Mohammedy and M. J. Deen, in *13 - Resonant cavity enhanced photodetectors: Theory, design and modeling*, ed. B. B. T.-P. Nabet, Woodhead Publishing, 2016, pp. 415–470, DOI: 10.1016/B978-1-78242-445-1.00013-0.

28 J. Li and M. Östling, in Photodetectors based on emerging materials, ed M. Rudan, R. Brunetti, S. Reggiani, *Springer Handbook of Semiconductor Devices. Springer Handbooks*. Springer, Cham, 2023, 777–805, DOI: 10.1007/978-3-030-79827-7_21.

29 J. Wang, H. Fang, X. Wang, X. Chen, W. Lu and W. Hu, Recent progress on localized field enhanced two-dimensional material photodetectors from ultraviolet—visible to infrared, *Small*, 2017, **13**, 1700894, DOI: 10.1002/smll.201700894.

30 M. A. H. Pappu, M. I. R. Ebon and J. Hossain, Design and simulation of $BeSiP_2$-based high-performance solar cell and photosensor, *Sol. Energy*, 2024, **279**, 112837, DOI: 10.1016/j.solener.2024.112837.

31 Y. Liu, D. Cadavid, M. Ibáñez, J. De Roo, S. Ortega, O. Dobrozhan, M. V. Kovalenko and A. Cabot, Colloidal $AgSbSe_2$ nanocrystals: surface analysis, electronic doping and processing into thermoelectric nanomaterials, *J. Mater. Chem. C*, 2016, **4**, 4756–4762, DOI: 10.1039/C6TC00893C.

32 S. Chen, X. Qiao, F. Wang, Q. Luo, X. Zhang, X. Wan, Y. Xu and X. Fan, Facile synthesis of hybrid nanorods with the Sb_2Se_3/$AgSbSe_2$ heterojunction structure for high performance photodetectors, *Nanoscale*, 2016, **8**, 2277–2283, DOI: 10.1039/C5NR06384A.

33 A. Kuruvilla, M. Francis and M. Lakshmi, Preparation of Single Phase of $AgSbSe_2$ from Sb_2Se_3/Se/Ag Stack, *Arab. J. Sci. Eng.*, 2023, **48**, 8115–8126, DOI: 10.1007/s13369-022-07488-9.

34 M. C. Islam, B. K. Mondal, M. A. H. Pappu and J. Hossain, Numerical evaluation and optimization of high sensitivity $Cu_2CdSnSe_4$ photodetector, *Heliyon*, 2024, **10**, e36821, DOI: 10.1016/j.heliyon.2024.e36821.

35 J. Hossain, B. K. Mondal and S. K. Mostaque, Design of a highly efficient FeS_2-based dual-heterojunction thin film solar cell, *Int. J. Green Energy*, 2022, **19**, 1531–1542, DOI: 10.1080/15435075.2021.2011291.

36 J. Hossain, Design and simulation of double-heterojunction solar cells based on Si and GaAs wafers, *J. Phys. Commun.*, 2021, **5**, 085008, DOI: 10.1088/2399-6528/ac1bc0.

37 M. J. Hossain, T. Jahan, J. Hossain and M. Hossain, Numerical simulation of all-inorganic two-terminal AlSb/$Al_{0.15}Ga_{0.85}Sb$ tandem solar cell with high-open circuit voltage (>1.90 V) and >40% conversion efficiency, *Sol. Energy Mater. Sol. Cells*, 2023, **263**, 112595, DOI: 10.1016/j.solmat.2023.112595.

38 P. R. Guddeti, P. M. B. Devi and K. T. R. Reddy, Optical and electrical investigations on Cu_2SnS_3 layers prepared by two-

stage process, *Chin. J. Phys.*, 2020, **67**, 458–472, DOI: 10.1016/j.cjph.2020.08.003.

39 L. M. M. Livingston, A. G. S. Raj, R. T. Prabu and A. Kumar, Computational analysis of FeS_2 material for solar cell application, *Opt. Quantum Electron.*, 2023, **55**, 244, DOI: 10.1007/s11082-022-04531-9.

40 A. Ennaoui, S. Fiechter, C. Pettenkofer, N. Alonso-Vante, K. Büker, M. Bronold, C. Höpfner and H. Tributsch, Iron disulfide for solar energy conversion, *Sol. Energy Mater. Sol. Cells*, 1993, **29**, 289–370, DOI: 10.1016/0927-0248(93)90095-K.

41 M. J. Nayeen, B. K. Mondal, S. R. Basu and J. Hossain, Theoretical exploration of high V_{OC} in Cu_2SnS_3 thin film solar cells towards high efficiency, *Sol. Energy*, 2023, **265**, 112076, DOI: 10.1016/j.solener.2023.112076.

42 I. Y. Kim, J. Y. Lee, U. V. Ghorpade, M. P. Suryawanshi, D. S. Lee and J. H. Kim, Influence of annealing temperature on the properties and solar cell performance of Cu_2SnS_3 (CTS) thin film prepared using sputtering method, *J. Alloys Compd.*, 2016, **688**, 12–17, DOI: 10.1016/j.jallcom.2016.06.264.

43 B. K. Mondal, Performance evaluation of $CuSbX_2$ (X = S, Se)-based 2T tandem solar cells towards high efficiency, *Opt. Mater. Express*, 2025, **15**, 2198–2215, DOI: 10.1364/OME.573214.

44 M. A. H. Pappu, S. N. Shiddique, B. K. Mondal, M. I. R. Ebon, T. Ahmed and J. Hossain, Numerical simulation on an efficient n-CdS/p-$ZnSnN_2$/p^+-Cu_2SnS_3/p^{++}-$CuGaSe_2$ thin film solar cell, *Mater. Today Commun.*, 2024, **38**, 108474, DOI: 10.1016/j.mtcomm.2024.108474.

45 H. Choi, J. Y. Seo, Y. R. Uhm, G. M. Sun and C. S. Kim, Crystalline structure and magnetic properties of pyrite FeS_2, *AIP Adv.*, 2021, **11**, 2–7, DOI: 10.1063/9.0000110.

46 M. Onoda, X. Chen, A. Sato and H. Wada, Crystal structure and twinning of monoclinic Cu_2SnS_3, *Mater. Res. Bull.*, 2000, **35**, 1563–1570, DOI: 10.1016/S0025-5408(00)00347-0.

47 C. K. Gan, J. R. Soh and Y. Liu, Large anharmonic effect and thermal expansion anisotropy of metal chalcogenides: the case of antimony sulfide, *Phys. Rev. B: Condens. Matter Mater. Phys.*, 2015, **92**, 23–26, DOI: 10.1103/PhysRevB.92.235202.

48 M. Burgelman, P. Nollet and S. Degrave, Modelling polycrystalline semiconductor solar cells, *Thin Solid Films*, 2000, **361**, 527–532, DOI: 10.1016/S0040-6090(99)00825-1.

49 M. Burgelman, J. Verschraegen, S. Degrave and P. Nollet, Modeling thin-film PV devices, *Prog. Photovoltaics Res. Appl.*, 2004, **12**, 143–153, DOI: 10.1002/pip.524.

50 U. Ur Rehman, N. Almousa, K. Ul Sahar, A. Ashfaq, K. Mahmood, E. A. Shokralla, M. S. Al-Buriahi, Z. A. Alrowaili, R. Y. Capangpangan and A. C. Alguno, Optimizing the efficiency of lead-free Cs_2TiI_6-based double halide perovskite solar cells using SCAPS-1D, *Energy Technol.*, 2023, **11**, 1–11, DOI: 10.1002/ente.202300459.

51 M. Loeza-Poot, R. Mis-Fernández, E. Camacho-Espinosa and J. L. Peña, Physico-chemical analysis of the properties and stability of CdS and CdS:O to be applied in thin-film solar cells, *Appl. Surf. Sci.*, 2024, **662**, 160125, DOI: 10.1016/j.apsusc.2024.160125.

52 T. Namitha Asokan and B. Pradeep, A study on reactively evaporated chalcogenide thin films for optoelectronic and thermoelectric energy conversion, *Diss. Cochin University of Science and Technology* (2017). https://dyuthi.cusat.ac.in/xmlui/handle/purl/5298.

53 J. He, J. Xu, X. Tan, G.-Q. Liu, H. Shao, Z. Liu, H. Jiang and J. Jiang, Synthesis of SnTe/$AgSbSe_2$ nanocomposite as a promising lead-free thermoelectric material, *J. Mater.*, 2016, **2**, 165–171, DOI: 10.1016/j.jmat.2016.05.001.

54 S. N. Guin, D. S. Negi, R. Datta and K. Biswas, Nanostructuring, carrier engineering and bond anharmonicity synergistically boost the thermoelectric performance of p-type $AgSbSe_2$-ZnSe, *J. Mater. Chem. A*, 2014, **2**, 4324–4331, DOI: 10.1039/c3ta14901c.

55 M. Kaifi and S. Gupta, Simulation of Perovskite based Solar Cell and Photodetector using SCAPS Software, *J. Eng. Res. Technol.*, 2019, **10**, 1778–1786.

56 S. A. Sayeem, M. A. Siddika, S. R. Basu, B. K. Mondal and J. Hossain, Numerical expedition on the potential of AgBiS2-based thin film solar cells employing different carrier transport layers, *ACS Omega*, 2024, **9**, 35490–35502, DOI: 10.1021/acsomega.4c02375.

57 M. H. Tonmoy, S. N. Shiddique, A. T. Abir and J. Hossain, Design and optimization of a high efficiency CdTe–$FeSi_2$ based double-junction two-terminal tandem solar cell, *Heliyon*, 2024, **10**, e27994, DOI: 10.1016/j.heliyon.2024.e27994.

58 B. K. Mondal, M. A. Newaz, M. A. Rashid, K. M. Hossain, S. K. Mostaque, M. F. Rahman, M. H. K. Rubel and J. Hossain, Electronic structure of $In_{3-x}Se_4$ electron transport layer for chalcogenide/p-Si heterojunction solar cells, *ACS Omega*, 2019, **4**, 17762–17772, DOI: 10.1021/acsomega.9b02210.

59 T. Watahiki, Y. Kobayashi, T. Morioka, S. Nishimura, D. Niinobe, K. Nishimura, H. Tokioka and M. Yamamuka, Analysis of short circuit current loss in rear emitter crystalline Si solar cell, *J. Appl. Phys.*, 2016, **119**, 204501, DOI: 10.1063/1.4951003.

60 D. Parajuli, D. K. Shah, D. KC, S. Kumar, M. Park and B. Pant, Influence of doping concentration and thickness of regions on the performance of InGaN single junction-based solar cells: a simulation approach, *Electrochem*, 2022, **3**, 407–415, DOI: 10.3390/electrochem3030028.

61 M. A. H. Pappu, A. Kuddus, B. K. Mondal, A. T. Abir and J. Hossain, Design of n-CdS/p-$CuInTe_2$/p^+-MoS_2 thin film solar cell with a power conversion efficiency of 34.32%, *Opt. Continuum*, 2023, **2**, 942, DOI: 10.1364/OPTCON.486044.

62 B. K. Mondal, A. T. Abir and J. Hossain, Current remedy in ultrathin crystalline Si solar cell by Cu_2SnS_3 thin film toward high efficiency, *Energy Technol.*, 2024, **12**, 2301329, DOI: 10.1002/ente.202301329.

63 S. G. Kumar and K. S. R. K. Rao, Physics and chemistry of CdTe/CdS thin film heterojunction photovoltaic devices: fundamental and critical aspects, *Energy Environ. Sci.*, 2014, **7**, 45–102, DOI: 10.1039/C3EE41981A.

64 S. R. Basu, M. I. R. Ebon, B. K. Mondal and J. Hossain, Theoreticalrevelation of Cu_3BiS_3 -based thin film pv cell exerting various carrier transport layers, *Adv. Theory Simulations*, 2025, **8**, 2401028, DOI: 10.1002/adts.202401028.

65 M. Z. Farah Khaleda, B. Vengadaesvaran and N. A. Rahim, in *Chapter 18 - Spectral response and quantum efficiency evaluation of solar cells: a review*, ed S. J. Dhoble, N. T. Kalyani, B. Vengadaesvaran, A. B. T.-E. M. Kariem Arof, Elsevier, 2021, pp. 525–566, DOI: 10.1016/B978-0-12-823710-6.00014-5.

66 B. K. Mondal, S. K. Mostaque, M. A. Rashid, A. Kuddus, H. Shirai and J. Hossain, Effect of CdS and In_3Se_4 BSF layers on the photovoltaic performance of PEDOT:PSS/n-Si solar cells: Simulation based on experimental data, *Superlattices Microstruct.*, 2021, **152**, 106853, DOI: 10.1016/j.spmi.2021.106853.

67 A. T. Abir, B. K. Mondal and J. Hossain, Exploring the potential of GeTe for the application in Thermophotovoltaic (TPV) cell, *Phys. Scr.*, 2023, **98**, 125940, DOI: 10.1088/1402-4896/ad0945.

68 J. Hossain, M. M. A. Moon, B. K. Mondal and M. A. Halim, Design guidelines for a highly efficient high-purity germanium (HPGe)-based double-heterojunction solar cell, *Opt. Laser Technol.*, 2021, **143**, 107306, DOI: 10.1016/j.optlastec.2021.107306.

69 M. Fortes, E. Comesaña, J. A. Rodriguez, P. Otero and A. J. Garcia-Loureiro, Impact of series and shunt resistances in amorphous silicon thin film solar cells, *Sol. Energy*, 2014, **100**, 114–123, DOI: 10.1016/j.solener.2013.11.022.

70 S. Upadhyay and D. Singh, Effect of series and shunt resistance on the performance of kesterite solar cells, *Int. J. Sci. Res. Mod. Sci. Technol.*, 2023, **2**, 38–45, DOI: 10.59828/ijsrmst.v2i8.134.

71 A. D. Dhass, Y. Prakash and K. C. Ramya, Effect of temperature on internal parameters of solar cell, *Mater. Today Proc.*, 2020, **33**, 732–735, DOI: 10.1016/j.matpr.2020.06.079.

72 Ferdiansjah, Faridah and K. T. Mularso, in Analysis of back surface field (BSF) performance in p-type and n-type monocrystalline silicon wafer, *E3S Web Conf.*, 2018, **43**, 0100, DOI: 10.1051/e3sconf/20184301006.

73 S. N. Shiddique, B. K. Mondal and J. Hossain, Modeling of $Ag3AuS_2$-based NIR photodetector with $BaSi_2$ BSF layer for superior detectivity, *Opt. Continuum*, 2025, **4**, 649, DOI: 10.1364/OPTCON.551703.

74 M. Islam, M. Pappu, T. Ahmed and J. Hossain, Theoretical sagacity of an efficient $Cu_2ZnGeSe_4$-based thin film solar cell and photodetector, *Adv. Theory Simulations*, 2025, **8**, e01272, DOI: 10.1002/adts.202401272.

75 M. A.-A. Arif, M. A. H. Pappu, A. T. Abir and J. Hossain, Numerical analysis of ternary chalcopyrite-type $ZnGeAs_2$-based photosensor and solar cell, *Opt. Continuum*, 2025, **4**, 1351–1367, DOI: 10.1364/OPTCON.561175.

76 M. S. Mollah, M. A. H. Pappu and J. Hossain, Theoretical design and insight of Fe_2GeS_4-based optoelectronic devices, *Next Res.*, 2025, **2**, 100575, DOI: 10.1016/j.nexres.2025.100575.

77 M. S. Gohor, M. I. R. Ebon and J. Hossain, A Comprehensive Study on $CdGeP_2$-based photonic device for dual applications in solar cell and photodetector, *Adv. Mater. Sci. Eng.*, 2025, **2025**, 9385403, DOI: 10.1155/amse/9385403.

78 S. N. Shiddique, A. T. Abir, S. S. Nushin, B. K. Mondal and J. Hossain, Numerical probing into the role of experimentally developed ZnTe window layer in high-performance Ag_3AuSe_2 photodetector, *Results Mater.*, 2025, **25**, 100651, DOI: 10.1016/j.rinma.2024.100651.